

UNIVERSITY OF EDINBURGH
SCHOOL OF PHYSICS AND ASTRONOMY



MPHYS PROJECT REPORT: 2022-23

**Structural properties of van der Waals
Ferromagnet: VI_3**

Authors

Boaz Ato MICAH

Supervisors

Dr. Chris STOCK

April 4, 2023

Abstract

Two-dimensional(2D) van der Waals ferromagnets are rare systems with special importance due to their potential to enable the architecture of the next-generation electronic devices. The recently discovered vanadium iodide (VI_3) ferromagnetic phase belongs to this family. VI_3 is reported to become ferromagnetic around 49 K. In this study, VI_3 was seen to undergo structural phase transition around 80 K, in agreement with already existing reports. However, there have been contradictory reports showing different crystal structures of VI_3 at both high and low temperatures, limiting the full understanding of its properties. Here, the crystal structure of VI_3 was investigated at high and low temperatures. The $R\text{-}3$ rhombohedral space group was the best-fitted space group at 100 K, and the $C2/c$ monoclinic space group best fits the powder X-ray data at 60 K, 28 K and 12 K. It was also observed that VI_3 does not undergo another structural transition around 32 K, as reported by other studies. The symmetry lowering of the crystal structure with temperature was also confirmed by peak splitting. The ferromagnetism in VI_3 is attributed to the distorted local crystalline electric field of the V^{3+} combined with their spin-orbit coupling. This provides the needed magnetic anisotropy for spatially long-range order.

1 Personal Statement

The X-ray diffractometer needed to obtain the powder diffraction was not ready until early November. From the beginning of the first semester until November, I had regular meetings with my supervisor to learn about the project's background. My supervisor gave me a list of articles and books on the project, and I familiarised myself with the content. Also, my supervisor advised me that the analysis would be done in MATLAB. I also began learning the syntax of MATLAB during this period, as I mostly program in python.

We started measuring the X-ray diffraction pattern at the beginning of November when the diffractometer was ready to use. We also started preparing our powdered sample during this period. It takes approximately two weeks to prepare the sample. Preparing the sample and obtaining the data took up to the middle of December to complete.

Afterwards, I began the analysis in early January by writing MATLAB code to observe a structural transition in the sample. The analysis for this part of the project was fairly straightforward and was completed in about a week. I also took on a side project of writing a python script that simulates magnetic order in a two-dimensional system.

Next, the main part of the analysis involved determining the crystal structure of the compound at high and low temperatures. To do this, we decided to use the JANA2020 software. Initially, I found the software very hard to use as it requires a thorough understanding of crystallography, and the interface is not very friendly. I spent most of January working through the different sets of data provided on their website and following the manual step-by-step. I found out that the manual provided for the dataset that is similar to our measured data does not work. I spent a lot of time trying to find the sequence of steps that work for our diffraction pattern. I finally managed to achieve this by early February. However, the refinement was imperfect, and some parameters were out of range. This led us to realise that our diffraction pattern will be very difficult to refine to the accuracy we desire. Initially, I tried the refinement process with different types of crystal structures, but this did not improve the issue. I also tried mixing different structures but to no avail. I tried many different sequences and sets of parameters to use in the refinement process. None of them improved the refinement noticeably. I documented each refinement process to reproduce the results if needed. At this point, we have already found the right crystal structure at high and low temperatures, with the values of all the parameters in a reasonable range. Further refinements were being done to improve the performance of the model. We hypothesised that the issue might be coming from the software. We decided to try a different software called Topas in early March. I quickly learnt the framework of the new software as I have now become comfortable with the whole process of structure determination. Surprisingly, the results from Topas are strikingly similar to the refinement models from JANA. This confirmed that the issue is from the diffraction data, and we concluded that the sample has a preferred orientation. The next step of this project is to measure the diffraction data using a diffractometer with a transmission geometry. This will eliminate the effects of preferred orientation. I have massively enjoyed this project and learnt a lot about the process of assigning a crystal structure to a material.

2 Acknowledgement

I sincerely thank my supervisor, Dr. Chris Stock, for his unwavering support and guidance during this project. I really appreciate the opportunity given by my supervisor to have given me access to the X-ray and sample preparation lab and, most importantly, his valuable time throughout. Without his guidance, the progress of this project would not have been possible, and I owe him a big thanks for his timely and consistent support. Chris' has a vast knowledge and understanding of two-dimensional materials that have helped me immensely to delve deeper into learning and understanding the fundamental physics of this topic. I would also like to thank Dr. Guratinder Kaur for using her expertise in refinement software to guide me during the analysis process and for providing constant and valuable feedback on my results. I learnt immensely from her and she was there everytime whenever I needed her help. I owe her a very big thanks.

Finally, I would like to thank my grandmom, Salomey Abrafi, my mom, Theresa Boateng, my sister, Emmanuella Hackman and my brother Samuel Micah for their unending love in my life.

Contents

1 Personal Statement	1
2 Acknowledgement	2
3 Introduction	3
4 Scientific Background	6
4.1 Diffraction Theory	6
4.2 X-ray Diffractometer	8
4.3 Diffraction Intensities	10
4.3.1 Structure form factor	10
4.3.2 Effect of multiplicity on intensity	12
4.3.3 Lorentz factor	12
4.3.4 Effect of temperature on the measured intensity	12
4.3.5 Peak shape broadening	13
4.4 Symmetry and Space Groups	14
4.5 Single-ion Hamiltonian	16
5 Experimental section	18
5.1 Sample preparation	18
6 Data Analysis	20
6.1 Rietveld Method	20
7 Results	22
7.1 Peak Splitting	22
7.2 Crystal structure of VI ₃ above the structural phase transition temperature	24
7.3 Crystal structure of VI ₃ below the structural phase transition temperature	28
7.3.1 Structural refinement at 60 K	29
7.3.2 Structural refinement at 28 K	30
7.3.3 Structural refinement at 12 K	32
8 Discussion	34
8.1 Preferred Orientation	34
9 Conclusion	35
Appendices	39
A Steps of performing Rietveld refinement with Jana2020 for 100K X-ray data	39
B MATLAB code for tracking the temperature dependence of the splitting peak with 2θ	46
C Lorentz fitting function with linear background	48

D Plot of the splitting peak at 100 K, 60 K, 28 K and 12 K	49
E Simulation of the two dimensional Ising model	50

3 Introduction

Ever since the successful isolation of a single sheet of graphene from bulk graphite in 2004 [1], research into two-dimensional(2D) materials, where the layers are held by van der Waals (vdW) forces, has attracted a lot of research interest. This is mainly driven by the compelling properties of the individual atomic layers. 2D materials continue to be the focus of intense research efforts serving as a platform for studying 2D physics. With these materials, novel heterostructure devices such as tunnelling transistors, resonant tunnelling diodes and light emitting diodes have been discovered[2]. These devices use the properties of 2D materials to create functionalities that are not accessible in other heterostructures. Despite the research effort, there are still an array of predicted 2D materials awaiting discovery [3, 4, 5, 6]. 2D materials have properties that are strikingly different from their 3D parent compound [7] such as; graphene is a gapless semiconductor[8], whereas graphite is a semi-metal with a band overlap [9]. Also, it has been well documented that the electrical, optical and magnetic properties can dramatically change at the few-layer thickness regime[10]. Depending on the constituting elements, the crystal structure, and even the relative angles between two layers, 2D materials can display a wide variety of properties ranging from metallic, semi-metallic, semiconducting and insulating behaviour [1]. As the family of 2D materials is expanding day by day, so too is the complexity of the heterostructures that could be created. The vdW bonding between the layers allows for these materials to be transferred onto a wide variety of substrates, enabling easy integration with silicon technology that is technologically mature [1]. Another immense benefit of 2D materials is the ability to tune their properties using an electric field in ways that are not possible for 3D materials due to their reduced dielectric screening [11].

Until recently, intrinsic long-range magnetic order remained elusive and was missing from the 2D family. The first evidence of 2D magnetism was proven in monolayers of CrI₃ and on a bilayer of Cr₂Ge₂Te₆ in 2017 [12][13]. 2D magnets are of great interest due to numerous reasons. First, the electronic and mechanical properties of 2D materials can be tuned using an electric field or strain, permitting the conception of devices where magnetic order is controlled at will, such as spintronic devices [14]. Second, they will serve as an avenue to deepen our understanding of magnetism. Third, magnetic order adds new functionality to the set of Lego-like pieces that enrich the game of vertical stacking of 2D vdW materials. The combination of materials with magnetic order and other 2D materials like graphene will probably result in structures with completely new and unexpected properties that we can explore theoretically and experimentally. The long wait in discovering magnetic 2D materials was surprising because layered vdW bonded magnetic crystals have been available for a long time [15] [16]. Hence, it should be possible to exfoliate the crystal down to one atomically thin layer. Indeed, some theoretical efforts had been made to demonstrate that such crystals would be stable and exhibit a finite critical temperature[17, 18].

Magnetism is realised when there is an ordered arrangement of magnetic moments (spins) over macroscopic length scales. This is typically driven by the interaction between neighbouring spins (exchange coupling) that tends to favour a specific relative orientation between them. At zero temperature (T), this local order extends over macroscopic length scales and there is a magnetic order. With increasing T, thermal fluctuations tend to

misalign magnetic moments in neighbouring regions, destroying long-range order above a certain critical temperature T_c . The effectiveness of thermal fluctuations determines whether a system undergoes a magnetic phase transition (ordered magnetic spins to disordered magnetic spins) at a finite T_c , and this is determined by a few parameters irrespective of the details of the system under consideration. In particular, dimensionality plays an essential role in determining the impact of thermal fluctuations [19]. The two dimensionalities of importance are the spin dimensionality, n , and the lattice dimensionality, D . The spin dimensionality of $n = 1, 2$ or 3 indicates whether the spin can occupy one-dimensional (1D), two-dimensional or three-dimensional (3D) space. The lattice dimensionality, D , specifies the dimension of the system.

In a 3D lattice system, a magnetic phase transition can always occur at a finite temperature, whereas in the 1D case, long-range order is only possible at zero kelvin [20]. The situation for 2D is complex and depends on the spin dimensionality and on the strength of the magnetic anisotropy.

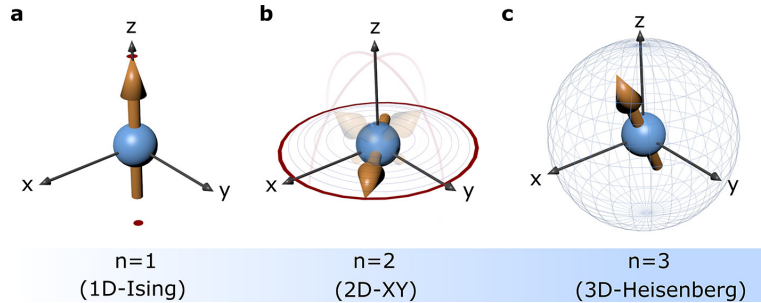


Figure 1: An illustration of the spin dimensionality in a 2D system. In the 1D Ising model, the spins can only point up and down, in the XY model, the spins can only in the X-Y plane and in the 3D-Heisenberg model, the spins can point in any direction in 3D space. The image for this illustration is obtained from [19]

Now, the spin dimensionality of any 2D material is $n = 3$, that is, Heisenberg isotropic, and the corresponding Hamiltonian is:

$$H = \sum_{i,j} J_{ij} \vec{S}_i \cdot \vec{S}_j \quad (1)$$

where the sum is over all nearest atoms, $J_{i,j}$ is the exchange coupling between neighbouring spins and \vec{S}_i , \vec{S}_j are the spins of the atoms. The Mermin-Wagner theory states that long-range magnetic order in an ideal Heisenberg 2D magnetic system is prevented by thermal fluctuations.[21]. This explains why it has been difficult to produce 2D magnets. These systems are easily excited at any finite temperature, with detrimental effects on magnetic order. In order for the 2D system to have magnetic order, it needs to have an extra term in its Hamiltonian, with a spin dimensionality of $n = 1$. The magnetic anisotropy of this term also needs to be strong to overcome the effects of thermal fluctuations. In the presence of the anisotropy, the Hamiltonian becomes:

$$H = \sum_{i,j} J_{ij} \vec{S}_i \cdot \vec{S}_j + \sum_i D S_{i,z}^2 \quad (2)$$

where the sum of the second term is over all atoms, D is the strength of the magnetic anisotropy and $S_{i,z}$ is the z-component of the spin. Onsager provided the exact solution of the ideal 2D-Ising model, which shows that a magnetic phase transition occurs at a finite temperature [22]. In this system, the anisotropy favours a specific spin component and suppresses the effect of thermal fluctuations. The images below show a snapshot of a simulation of the equilibrium states of the Ising model above and below the critical temperature using Glauber dynamics[23]. This simulation contains 100 by 100 lattice spins. Yellow squares represent the up spins, and the down spins are shown as purple squares.

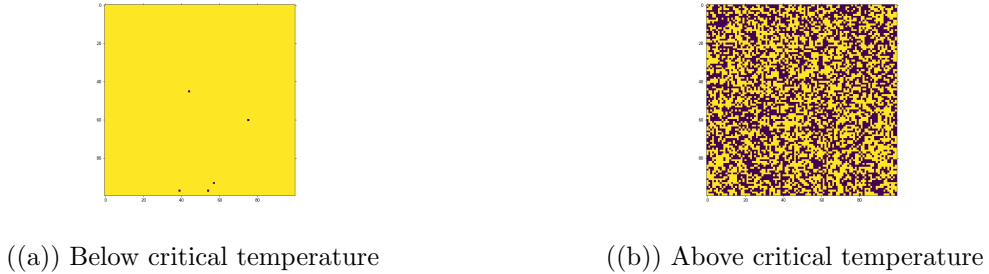


Figure 2: Snapshot of the simulation of the 1-D Ising model; above and below the critical temperature using Glauber dynamics.

As seen from Figure 2, below the critical temperature, the spins are aligned in a preferred direction(up direction in this case), whereas the spins are disordered in the high-temperature regime.

In this study, we report a layered ferromagnetic semiconductor, vanadium iodide (VI_3). The existence of VI_3 was first reported in 1969, where the unit cell dimensions and space group were described but no detailed crystallographic results are available[24]. Afterwards, the compound has been largely ignored until the recent surge in discovering 2D magnetic materials. Several reports have confirmed the existence of ferromagnetism down to the monolayer in VI_3 below 50 K [25][26]. It is also reported to undergo structural transition at a higher temperature of around 79 K [27]. A number of studies have reported the crystal structure of the compound in high and low-temperature regimes. However, there have been contradictory statements. Reference [28] report the room temperature (RT) trigonal structure $P31c$ and a monoclinic crystal structure at low temperatures (LT). Reference [29] determined the trigonal structure $R-3(148)$ at 100 K and suggested a subtle structural phase transition. In contrast, reference [25] claim a high temperature (HT) monoclinic structure $C2/m$ (determined at 100K) and the LT rhombohedral structure $R-3$ (determined at 60 K and 40 K). Interestingly, all these reports agree on the same structural transition temperature of around 79 K. The inconclusiveness of determining the crystal structure of VI_3 has limited our full understanding of its properties and its potential as a monolayer magnetic material.

This report is about the study of the crystal structure of VI_3 using X-ray diffraction as a function of temperature. The steps in this project involve purifying VI_3 sample through sublimation and using an X-ray diffractometer to obtain the diffraction pattern at various temperatures. The pattern is then analysed using the Jana2020 software [30] to determine the crystal structures at the measured temperatures. VI_3 offers more opportunities to

study the ferromagnetism in layered structures and more possibilities in future 2D devices.

The motivation for this report are:

- Comprehensively determine the evolution of the crystal structure of VI_3 with temperature using powder X-ray diffraction.
- Determine the structural phase transition of VI_3 and confirm that this is the only structural transition it undergoes.
- Discussion of the presence of the long-range order in VI_3 .
- Finally, the single ion Hamiltonian of the V^{3+} ions makes a structural prediction at low temperature. The prediction requires two vanadium ions in the unit cell at low temperatures. This will also be investigated.

4 Scientific Background

4.1 Diffraction Theory

When an object is irradiated with some radiation, the scattered radiation carries information about the object. For a crystal material, the scattering contains enough information to determine the position of its atoms. A crystal is defined as any solid with an essentially ordered arrangement of atoms or molecules that extends in all three spatial directions and has a diffraction pattern of sharp spots. A crystal is built up by adding, in three dimensions, identical building blocks called a unit cell.

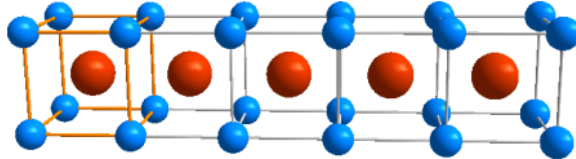


Figure 3: Periodic arrangement of unit cells in a crystal lattice [31]

Crystals usually have an inherited symmetry associated with them such that when the corresponding symmetry operation is applied, the position of the atoms remains unchanged. Symmetry operations impose restrictions on the unit cell's axis and angles. This project used powdered VI_3 to obtain the diffraction pattern. The powdered sample is comprised of very small crystallites. A crystal(or crystallite) comprises many sets of crystal planes extending completely through it. The crystal planes are a set of parallel planes on which all the atoms of a crystal can be located. Each set of planes can be identified using three indices (hkl) known as the Miller indices. Braggs's law [32], which gives the condition for diffraction, is based on these planes:

$$n\lambda = 2dsin\theta \quad (3)$$

where λ is the radiation wavelength used, d is the perpendicular spacing between a crystal plane, θ is the angle between the incident (or diffracted) ray and the crystal planes causing the diffraction and n is an integer, referred to as the order of diffraction. Considering

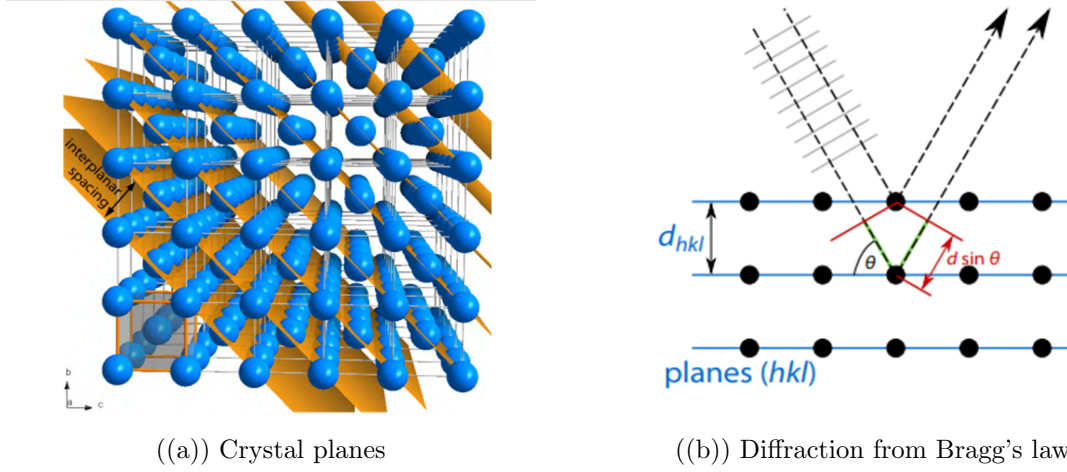
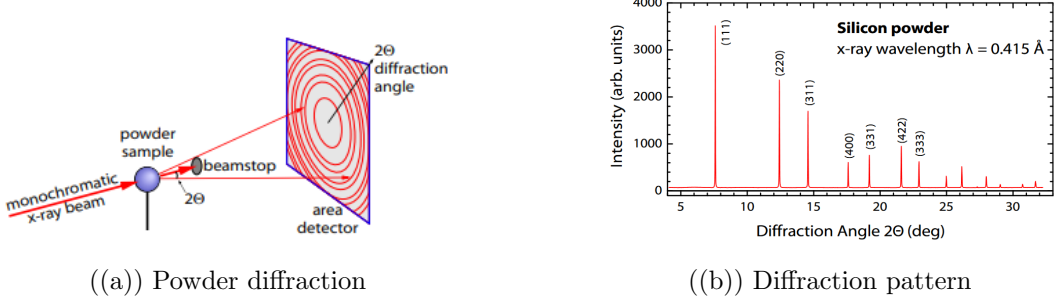


Figure 4: (a) An illustration of one set of crystal planes within a crystal. (b) A demonstration of Bragg's law in action. The images were obtained from [31]

the situation of an X-ray incident on a crystallite within a powder sample, there won't necessarily be a diffraction. Bragg's law shows that the crystallite must be correctly oriented with respect to the X-ray beam; that is, one of the sets of planes within the crystallite must be correctly oriented with respect to the X-ray beam to diffract (the atoms scattering in phase and producing an intense diffracted ray). In this particular direction, X-rays scattered from successive planes interact constructively, with a phase difference that equals an integer multiple of wavelengths. If the crystallite gets rotated, a second set of crystal planes might be correctly oriented with the X-ray beam to produce diffraction. The advantage of powder diffraction is that a proper powdered sample consists of millions of crystallites, each at different orientations. Hence, an incoming X-ray beam is exposed to every possible orientation for each set of crystal planes. Statistically, for each set of planes, there are bound to be some at the right orientation with respect to the X-ray beam. This prevents the need to grow a sufficiently large crystal or to obtain a sample rotation system. One concluding idea from Bragg's law is that diffraction is an "arranged event"; three parameters need to be harmonised: the wavelength of the X-rays, the crystal orientation and the inter-planar spacing between the crystal planes. One can fix two of these parameters and continuously change the third parameter until Bragg's law is satisfied in order to produce diffraction.

In powder diffraction, circular diffraction rings are observed on a detector. The rings originate from the superposition of millions of diffraction spots, each of them originating from an individual crystallite. Due to the fact that the crystallites are randomly oriented, each circle corresponds to an individual or overlapped set of crystal planes (reflections). The intensity associated to each plane is then obtained from integrating around the corresponding ring. This lets us obtain the powder diffraction pattern as a plot of diffracted intensity against diffraction angle, 2θ .



((a)) Powder diffraction

((b)) Diffraction pattern

Figure 5: An illustration of the powder X-ray diffraction process [31]

4.2 X-ray Diffractometer

This section focuses on the geometry of the X-ray diffractometer that was used to measure the diffraction pattern of the powder sample. The instrument used the reflection geometry setup, and a simple diagram is shown in Fig 6.

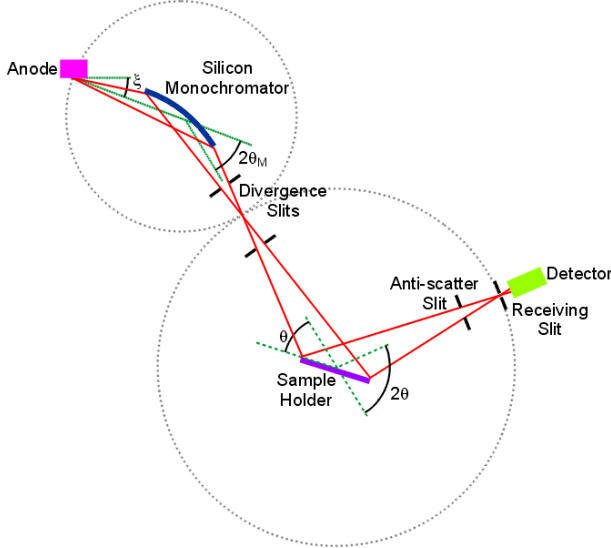
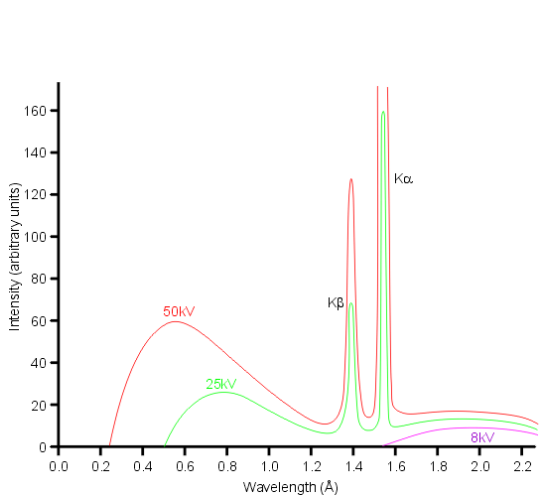
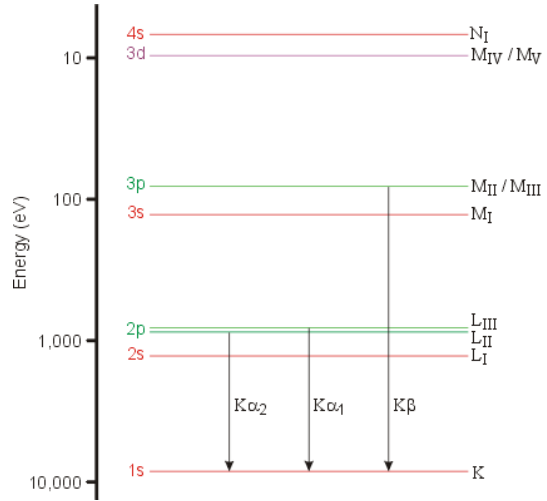


Figure 6: Reflection geometry setup of X-ray diffractometer [33]

The X-rays are generated in a sealed tube by heating a filament to produce electrons. A high electric field accelerates these electrons towards a copper target. The process is inefficient, with most of the beam's energy being dissipated as heat in the target. Some of the electrons lose energy by collisions with the atoms. This results in the emission of a continuous spectrum of X-rays known as white radiation in a process called bremsstrahlung [34]. The copper anode has an energy threshold above which a second type of spectrum is obtained superimposed on top of the white radiation. This is the characteristic radiation and is composed of discrete peaks. The discrete peaks occur when the electron has enough energy to eject an inner electron from the copper atom. This leads to a vacant orbital which is then filled by a higher energy electron, emitting an X-ray in the process. The energy of the X-ray photon is equal to the difference in energy between the two energy levels.



((a)) Typical X-ray spectrum from a copper target. The green line shows the white radiation and the characteristic radiation is shown by the red line.



((b)) The electronic energy levels for a copper atom

Figure 7: The X-ray spectrum from a copper target [35]

The next step is to select the $K\alpha_1$ wavelength as shown in Fig.7(b) from the X-ray spectrum using a monochromator. At higher resolutions, the $K\alpha$ peak in Fig.7(a) is split into the two peaks, $K\alpha_1$ and $K\alpha_2$. The monochromator is made up of lots of little crystals, all approximately aligned in the same orientation to form a mosaic. The distribution of the alignments of the blocks determines the spread of the crystal. The material used for the monochromator in this project is germanium. The monochromator works by the reflection of the wavelengths that obey Bragg's law for a specific d spacing of the monochromator. For a germanium crystal to select the $K\alpha_1$ wavelength, the crystals must be oriented at a specific $2\theta_M$ position. Monochromator crystals partially polarise the unpolarised X-ray beam from the sealed tube. In theory, the effect of polarization on the intensity of the diffraction pattern should be considered during data processing, but in practice; the correction effect is relatively small and often ignored [36].

Next, the divergence slits are used to control the direction of the incident and diffracted beam. In this reflective setup, both the X-ray source and the monochromator are fixed; only the sample and the detector rotate by θ and 2θ , respectively. The dotted circle centred on the sample position in Figure 6 represents the goniometer circle on which the divergent source X-rays are focused by diffraction from the flat-plate sample holder containing the powdered crystals.

The detector is a scintillation counter and converts X-ray photons into an electrical signal. The X-ray photon collides with the scintillator, and this produces long wavelength photons within the visible spectrum. A photomultiplier tube, connected to the scintillator, is then used to convert the photons into a voltage pulse. The number of electrons ejected is proportional to the number of visible photons which strike it, which is also proportional to the energy of the original X-ray photon. The generated voltage pulses are then recorded as intensity on computer software. The data acquisition process is a step scan approach in which the detector arm is moved to a specific 2θ , and the software

records the total number of counts for a given count time.

4.3 Diffraction Intensities

4.3.1 Structure form factor

The crystal plane is only an abstract mathematical concept used to explain diffraction; rather, it is the atoms within the crystal that scatter the X-rays. Bragg's law allows us to determine the unit cell dimensions from measured diffraction angles but yields no information on the relative intensities of the reflections from different crystal planes, which tends to be crucial for determining the positions of the atoms in the unit cell [32]. X-rays are scattered by the electrons in a crystal. The scattering strength at point r is dependent on the spatial distribution of electron charge at that point - the charge density $n(r)$. Let us consider an incoming electromagnetic plane wave entering and propagating through the crystal. At every point r within the crystal, there is a probability that the X-ray gets scattered into a secondary spherical wave, which scales with the electron density $n(r)$ at that point. In the classical picture, the electrons oscillate due to the electric field of the X-rays. The oscillating electrons then emit radiation in all directions. All the scattered contributions interfere in some way in the direction of the outgoing beam. This means the phase differences of all contributions need to be accounted for. In order to obtain a measure of the "diffraction strength", the integral of phase-weighted contributions over the whole crystal is obtained. This is known as the scattering amplitude of the crystal. The scattering amplitude assumes the scattering is elastic - the magnitude of the wave-vector of the incoming and scattered radiation is the same.

$$F(k, k') = \int_{\text{crystal}} n(r) e^{-i(k-k') \cdot r} dV \quad (4)$$

where $F(k, k')$ is the scattering amplitude of X-rays with incoming wavevector k and outgoing wavevector k' . $n(r)$ is the electron density distribution in the crystal. The dot product $(k - k') \cdot r$ represents the phase difference between the incident and scattered waves. The scattering amplitude describes the ratio of the diffracted and incoming electric field strength.

Every crystal has two lattices attached to it. The direct lattice and the reciprocal lattice. The direct lattice describes the periodicity of the atomic arrangement, and the reciprocal lattice is the Fourier space representation of the crystal.

In Fourier space, the scattering amplitude can be expressed as:

$$F(k, k') = \sum_G n_G \int_{\text{crystal}} e^{i[G - \Delta k] \cdot r} dV \quad (5)$$

where G is the reciprocal lattice points, n_G is the Fourier coefficients of the electron distribution function, and Δk is the difference between the incoming and outgoing wavevector. The integral in Eq(5) will always yield a value close to zero because the integral is over a rapidly oscillating function. The only exception is when $G - \Delta k$ is equal to zero. This yields the condition that diffraction only occurs in directions for which the scattering vector Δk equals a reciprocal lattice vector. In this way, one can associate every observed

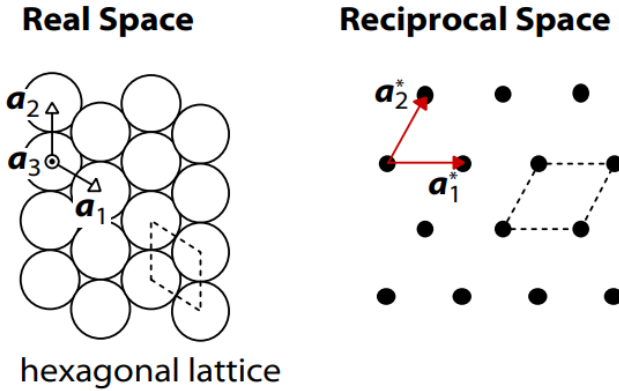


Figure 8: An hexagonal lattice in real space with lattices parameters of a_1 , a_2 and a_3 . A reciprocal space representation which is also hexagonal with lattice parameters of a_1^* , a_2^* and a_3^* [31].

diffraction spot with a reciprocal lattice vector. This condition is known as the Laue diffraction condition and has been proven to be equivalent to Bragg's law [37].

It must be noted that the scattering amplitude is the Fourier transform of the electron density of the crystal. The electron density of a crystal is usually unknown and is approximated by a superposition of free atom (or ion) electron densities. This approximation neglects the redistribution of the valence electrons due to chemical bonding, but it makes it possible to calculate diffraction intensities directly using only information about the types of atoms/ions in the unit cell and where they are located. The approximated scattering amplitude is known as the structure factor, and it is given as:

$$S_{hkl} \equiv S_G = \sum_j f_j e^{-i2\pi(hx_j + ky_j + lz_j)} \quad (6)$$

where the sum is the over the atoms in a unit cell , f_j (atomic form factor) is the Fourier transform of the electron density of a single free atom, h, k, l are the miller indices and x, y, z are the atomic positions. Every structure factor is a 3D Fourier of the electron density distribution. Hence, the diffraction process makes the Fourier coefficients almost measurable. The intensity is directly proportional to the modulus squared of the structure factor. Hence, the measured intensities allow for the position of the atoms to be determined. This explains why diffraction from different planes have varying intensities. The differing intensities is as a result of the difference in atomic form factor of the diffracting atoms.

The experimentally measured intensity will still be different from the structure factor due to a number of additional experimental effects such as the multiplicity, polarisation factor, Lorentz factor and X-ray absorption. The measured intensity can be expressed as:

$$I_{hkl} = c j L S_{hkl}^2 \quad (7)$$

where, c contains the effect of all remaining factors(amount of X-ray exposure, the sensitivity of the detector, polarization and absorption.), j is the multiplicity and L is the

Lorentz factor.

4.3.2 Effect of multiplicity on intensity

The multiplicity effect occurs when two or more different crystal planes have the same or similar d-spacing. When this happens, these sets of crystal planes will all contribute to the same diffraction peak, and it will be impossible to account for how much intensity comes from which plane. The experiment will record the sum of the intensities from each crystal plane within the set. This effect is accounted for by counting the number of equivalent planes that diffracts to the same 2θ angle. The multiplicity factor, j , accounts for this specific intensity effect from the powder sample.

4.3.3 Lorentz factor

Diffraction, as given by Bragg's law, does not occur at definite values of radiation wavelength, d-spacing and diffraction angle. All three values have an uncertainty over which diffraction could occur. Similarly, the reciprocal lattice points have a finite volume attached to them within the reciprocal lattice. This uncertainty attached to wavelength and inter-planar spacing is accounted for by the Lorentz factor. The Lorentz factor is geometry-dependent and changes with the experimental setup. For standard powder diffraction arrangements, the relationship between the Lorentz factor and the diffraction angle is given by [36]:

$$L = c / (\sin \theta \sin 2\theta) \quad (8)$$

where c is a constant. The plot of how the Lorentz factor changes with 2θ is shown below:

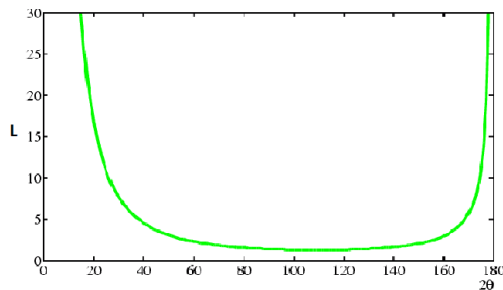


Figure 9: Shape of the graph of the Lorentz factor for standard powder diffraction arrangements [38]

The effect of the Lorentz factor is more pronounced at low and high diffraction angles.

4.3.4 Effect of temperature on the measured intensity

The structural factor derived in section 4.3.1 was based on the idea that the atoms were stationary. In reality, the atoms are constantly moving, and their displacements about their equilibrium position increase with temperature. The displacements will also be

different for different atoms. The displacement of an atom is coupled to the motion of many other atoms. Hence, the atomic form factor of an atom needs to be adjusted to take into account the broadening of the electron cloud resulting from the atomic motion. In practice, the coupled motion of the atoms is ignored, and one only considers the independent motion of an atom. With this, the atomic form factor of each atom or ion can be modified to take into account the displacement of the atom at the equilibrium position. An individual atom or ion will have its motionless atomic form factor, f , changed to f_T according to [36]:

$$f_T = f e^{-B \sin^2 \theta / \lambda^2} \quad (9)$$

where T is the temperature and $B = 8\pi^2 < u^2 >$ (units of Å), $< u^2 >$ is the root mean squared displacement of the atom from its average position. The B values are referred to as the thermal displacement parameters, and they increase with temperature. As seen, the temperature has an effect on the measured intensity by directly modifying the scattering amplitude. The effects of temperature are accounted for in a process called the Rietveld refinement discussed at section 6.1. In this process, the B values are refined in an iterative process in order to find the optimal B values that describe the measured intensities.

Also, we have made another assumption that the B values are the same in all directions, isotropic B values. In complex structures, each atom will have six B values describing their atomic displacements, anisotropic B values. The Rietveld refinement method can also account for this.

4.3.5 Peak shape broadening

Ideally, in a diffraction experiment satisfying Bragg's law, the diffracted peak should appear as a sharp line with intensity given by $|F_{hkl}|^2$ at a position 2θ . In practice, the diffraction peak is broadened and its intensity is modified as discussed above.

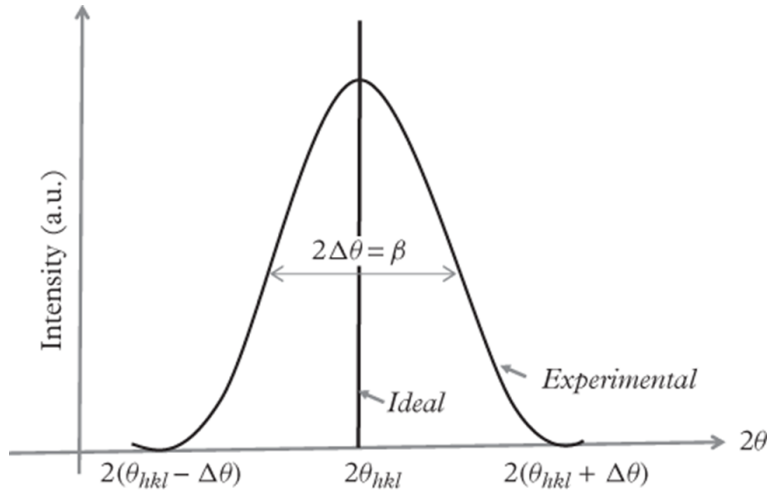


Figure 10: Broadening of a diffraction peak due to a variety of factors including the crystallite size, strain and instrument factors [36].

In this project, the Pseudo-Voigt function was used to describe the peak shapes. The

function is a combination of a Gaussian and a Lorentz and is given by:

$$I(2\theta) = I_{hkl}[\eta L(2\theta - 2\theta_0) + (1 - \eta)G(2\theta - 2\theta_0)] \quad (10)$$

where $I(2\theta)$ is the measured intensity, I_{hkl} is the expected intensity incorporating the structural factor and the effects of temperature, multiplicity, Lorentz factor, polarisation and absorption, η is the Lorentz fraction, $L(2\theta - 2\theta_0)$ and $G(2\theta - 2\theta_0)$ represent suitably normalised Lorentz and Gaussian functions.

Across the whole X-ray diffraction pattern, the peak width, β , varies with the diffraction angle. Meaning, to obtain the intensity across the whole pattern, the full width at half maximum of the Gaussian and Lorentz functions must be determined at each diffraction angle. The dependence of the peak broadening with θ is given in the formula below [39]:

$$\beta^2 = Utan^2\theta + Vtan\theta + W \quad (11)$$

In practice, the parameters, U , V and W are refined in an iterative process until the fitting function best describes the peak. The peak broadening arises from the instrument and sample contributions. These two effects are inter-dependent in the sense that any imperfection in one (for instance, just one imperfect powder crystallite) will in turn be subject, statistically, to all the imperfections of the instrument. Common sources of instrumental imperfection include the radiation not being perfectly monochromatic, misalignment of the diffractometer and axial divergence of the incident or diffracted beams. On the other hand, the crystallite size and strain are the biggest causing factors in sample imperfections.

4.4 Symmetry and Space Groups

As already stated, a crystal is a solid material made up of a repeating pattern of atoms, ions, or molecules. The way these units are arranged in space is described by the crystal structure, which can be divided into two main parts: the unit cell and the lattice. The unit cell is the smallest repeating unit of the crystal structure, while the lattice is the arrangement of these unit cells in space. The symmetries of crystal shapes reflect symmetries in the atomic arrangements. For diffraction to take place, crystals need to possess some translational symmetry. Symmetry links diffraction data to crystal structure. A symmetry operation is a geometrical operation that transforms an "object" to a state that is indistinguishable from the starting point, and this can be applied both to a crystal as a whole and the atomic arrangement within a crystal. Some symmetry operations include mirror, rotation, translation and inversion symmetry. In some cases, there are somewhat hidden symmetries that can be made more apparent by using a centred lattice. These centred lattices are primitive(no centring), face-centred (all three pairs of cell faces), body-centred (centred in the interior) and base-centred(one pair of cell faces). Symmetry operations restrict the lattice parameters of unit cells within a crystal. In three dimensions, there are seven crystal systems, each being defined by different symmetry requirements and the corresponding restrictions on the lattice parameters a, b, c and α, β, γ : cubic, tetragonal, orthorhombic, monoclinic, triclinic, hexagonal, and rhombohedral. The seven crystal systems can be combined with the four types of centring lattices giving 14 Bravais lattices.

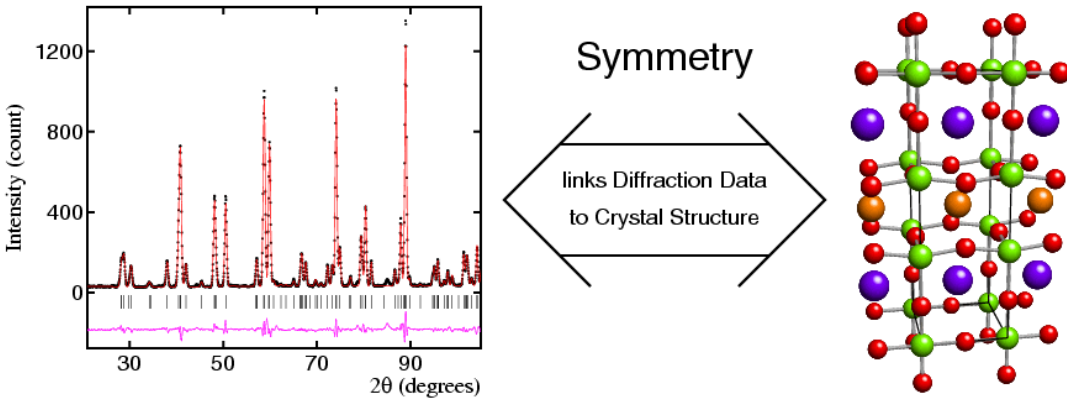


Figure 11: An illustration linking diffraction pattern to its crystal structure [40].

Crystal System	Centring	Restrictions on Unit Cell Properties	
Cubic	P, F, I	$a = b = c$	$\alpha = \beta = \gamma = 90^\circ$
Hexagonal	P, R	$a = b$	$\alpha = \beta = 90, \gamma = 120^\circ$
Trigonal		$a = b = c$	$\alpha = \beta = \gamma \leq 120^\circ, \neq 90^\circ$
Tetragonal	P, I	$a = b$	$\alpha = \beta = \gamma = 90^\circ$
Orthorhombic	P, I, F, C	none	$\alpha = \beta = \gamma = 90^\circ$
Monoclinic	P, C	none	$\alpha = \gamma = 90^\circ \neq \beta$
Triclinic	P	none	none

Figure 12: Restrictions on the 14 Bravais lattice [31]

A symmetry operator takes as input the coordinates of an atom and returns the coordinates of another atom. This operation represents the symmetry relation between the two atoms, such as a 180 degrees rotation about the z-axis. A symmetry group is a set of symmetry operators that follow the following rules [41]:

- The overall action of two symmetry operators must always be equivalent to the action of a single symmetry operator that belongs to the same group
- The identity symmetry operator must be within the group
- Each symmetry operator in the group must have an inverse operator belonging to the group

A point group is a group of symmetry operators(symmetry group) that keeps the position of one or more atoms stationary. Each point group has a set of symmetry operators attached to it. In crystallography, there are only 32 point groups with the seven crystal systems.

The total number of permutations of Bravais lattices with the point group symmetries is finite: there are only 230 unique combinations, and these combinations are known as the 230 space groups. A space group is any number of ways in which the orientation of a crystal can be changed without changing the position of its atoms, and it describes the inherent symmetry of the sample. A crystal can be assigned to one of these groups

after studying its diffraction pattern. The interesting effect of symmetric is that it can cause certain diffraction peaks to not exist within the diffraction pattern. These are called systematic absences. For instance, in a body-centred crystal structure, all reflections with odd $h + k + l$ are missing. The space group of a particular diffraction is determined using the lattice parameters (determined from the miller indices of the peak) and the reflection conditions within the data. With an assigned space group, the symmetry operations can be applied to the atomic coordinates of the unit cell to obtain the positions of all the atoms in the crystal. This project's main focus is to determine the space group of VI₃ at low and high temperatures.

4.5 Single-ion Hamiltonian

This section of the report is mainly from reference [42], which investigated the magnetic excitations of VI₃ in the context of the spin-orbital properties of V³⁺. This is included so as to compare the best-fitted space group at low temperature with the prediction made by the single ion Hamiltonian of V³⁺. Considering an isolated vanadium ion in VI₃, it has two electrons in its outer d orbital. This gives it a five-fold degeneracy with an orbital angular momentum of two. As already stated, VI₃ becomes ferromagnetic and also undergoes a structural distortion at low temperatures. The combination of the orbital degree of freedom, low-temperature crystalline distortion and ferromagnetism gives the following single-ion Hamiltonian terms:

$$H_{SI} = H_{CEF} + H_{SO} + H_{dis} + H_{MF} \quad (12)$$

where H_{SI} is the single ion Hamiltonian, H_{CEF} is the octahedral crystalline electric field, H_{SO} is the spin-orbit coupling, H_{dis} is the structural distortion away from a perfect octahedral and H_{MF} is the local molecular field imposed by the ferromagnetic order.

Starting from an isolated V³⁺ ion, let us consider the effect of introducing the Hamiltonian terms. In VI₃, the two electrons in the vanadium ion are surrounded by six iodide ions imposing a crystalline electric field on the V³⁺ ions. References [43][44] have discussed the single-ion properties of VI₃ using a strong crystal-field approach. They discovered that the electric field splits the five-fold d orbital degeneracy into a ground state triplet t_{2g} and excited state doublet e_g . The electric field fixes the magnetic ground state of VI₃ to have both an orbital angular momentum and a spin value of 1, that is, $|l = 1, S = 1\rangle$. As seen from Fig.13, the introduction of the crystal field leads to a lowering of the ground state. There are nine degenerate ground states at this level. The effect of the spin-orbit coupling on the $|l = 1, S = 1\rangle$ ground state with a Hamiltonian, $H = \alpha\lambda I \cdot S$ is shown in Fig.13. It splits the ground state into three different states with a total angular momentum of $J = 0, 1, 2$, respectively. The new ground state has a total angular momentum of $J = 2$. Hence, the introduction of spin-orbit coupling has reduced the degeneracy from nine to five. This is shown in the Fig. 13 as the three splitting lines in the spin-orbit section.

VI₃ distorts from an ideal octahedron at low temperatures. In reference [42], the Hamiltonian term for the distortion is given as:

$$H_{dis} = \tau(\hat{l}_z^2 - \frac{2}{3}) \quad (13)$$

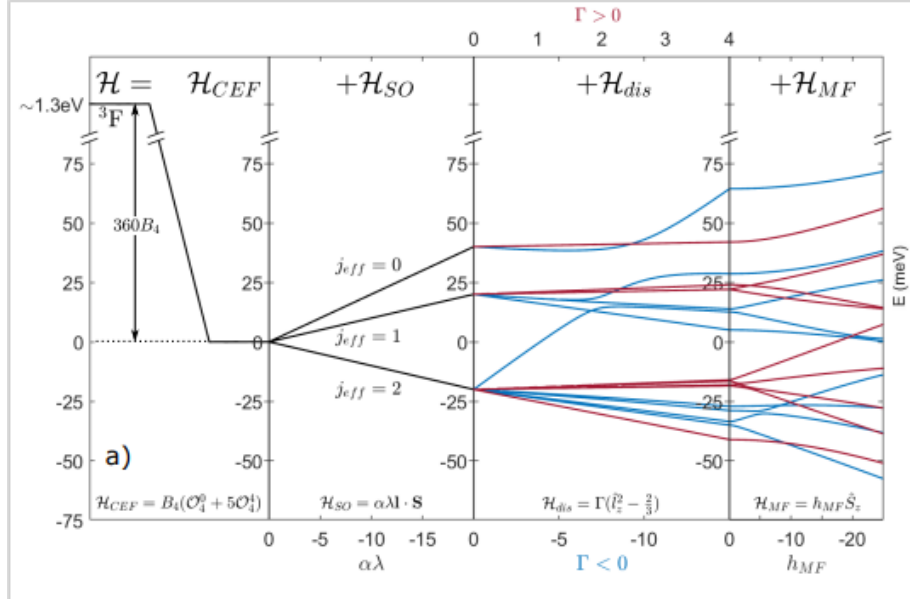


Figure 13: Energy of the V^{3+} ion under a crystal-field H_{CEF} , spin-orbit coupling H_{SO} , octagonal distortion H_{dis} , and mean molecular field H_{MF} . Positive and negative distortions are shown in red and blue, respectively.

where τ is proportional to strain and \hat{l}_z is the z-component of the angular orbital momentum.

This additional energy term causes further splitting of the ground state and, interestingly, results in two possible orbital ground states depending on the value of τ . When τ is less than zero, we get a flattened octahedron with an orbital ground state doublet. When τ is greater than zero, an elongated ground-state singlet. These two scenarios are shown in different colours in Fig. 13. The existence of two possible ground states in VI_3 at low temperatures signifies that the crystal structure should also have two vanadium ions at low temperatures. This means the best-fitted space group at low temperature must contain the atomic coordinates of two vanadium ions, from which the coordinates of all the vanadium ions in the crystal can be obtained. This hypothesis will be compared to the structural results of the measured X-ray powder data at low temperatures.

Lastly, the molecular field term, H_{MF} , which is present in the ferromagnetic phase from neighbouring ordered spins, induces a Zeeman field on the V^{3+} sites. This term splits the degenerate levels, as illustrated in the figure above.

5 Experimental section

5.1 Sample preparation

The powder crystals of VI_3 were prepared by the chemical vapor transport method[29]. Stoichiometric amounts of vanadium powder and iodine were loaded in ampoules and sealed in a vacuum. The ampoules were then put into a tube furnace with the hot end held at 400°C and the cold end at room temperature. After approximately two weeks of vapor transport, the ampoules were quenched, and shining black flake-like crystals were obtained, characteristic of two-dimensional layered systems. The ampoules were opened, and the crystals were crushed using mortar and pestle in an inert nitrogen gas glove box. The grinding was done in the nitrogen glove box as VI_3 is air sensitive, and water



Figure 14: VI_3 crystals prepared using chemical vapor transport. The crystals were crushed in a nitrogen glove box.

vapor can easily condense on the sample. The grinding was done for approximately two hours so as to avoid preferred orientation in the measured data. Preferred orientation is the phenomena that occurs in the diffraction pattern when the crystal planes are more likely to align in a particular direction than others. This affects the measured intensity of the pattern as powder diffraction is heavily dependent on the samples having random orientation. However, the effects of preferred orientation was not completely avoided in the measured diffraction and this will be discussed further. The grinding process of VI_3 is not very easy due to the fact that it is a layered structure.

The finely ground powder was then transferred to the Rigaku smart lab sample holder to measure the temperature dependence of VI_3 . Extra care was taken when transferring the sample to the sample holder, with a minimum amount of exposure to the environment. The Rigaku sample holder has a temperature range of 12 K to 300 K.

The powder X-ray pattern was measured at short scanning times for various temperatures and measured at long-scan times at 100K, 60K, 28K and 12K.

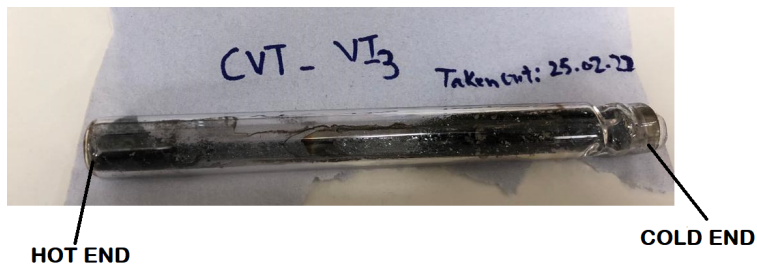


Figure 15: Shiny crystals of VI₃ in an ampoule made from the chemical vapor transport method.

6 Data Analysis

6.1 Rietveld Method

Single-crystal diffraction provides a direct approach to determining the crystal structure of a material [45]. However, when studying the crystal structure of a material over an extensive range of temperatures, the single crystal may be destroyed in the process. Powder X-ray diffraction allows this situation to be avoided completely. The main disadvantage of powder diffraction is that the three-dimensional diffraction data of a single crystal is compressed onto the diffraction angle 2θ , leading to an overlap of reflections from different crystal planes [46]. This overlap makes it difficult to sometimes assign a diffraction peak to a specific crystal plane in the structure. Often, multiple crystal planes or miller indices can be assigned to the same diffraction peak. This makes it difficult to determine the crystal structure of the diffraction pattern. The Rietveld method provides the solution to this problem by adopting a whole pattern-fitting approach. The Rietveld method works by creating a structural model. The structural model consists of parameters that define the space group, the peak shapes, the atomic coordinates in the unit cell, the atomic site occupancies, the lattice parameters, background parameters and many more. See Appendix A for the full list of the parameters that were used in the Rietveld method. The objective of the Rietveld refinement method is to match the intensity of the measured powder X-ray diffraction pattern at each value of 2θ as possible. This is achieved by using an iterative least-squared method where the structural model is used to calculate the intensity, $y_{calc,i}$, at each 2θ position and then compared to the measured intensity, $y_{obs,i}$. The difference between the two intensities is minimised by changing some parameters within the model. The minimised quantity is:

$$\sum_{i=1}^N w_i (y_{obs,i} - y_{calc,i}), \quad (14)$$

where w_i is the weight attributed to each observation. This is an iterative process where the model's parameters are slightly changed with each cycle, and the model's performance in matching the measured intensities improves(hopefully). The refined parameters are then used to improve the subsequent minimisation cycle. The performance of the refinement is followed by monitoring the goodness of fit (GoF) or χ quantity:

$$GoF = \chi = \sqrt{\frac{\sum_{i=1}^N w_i (y_{obs,i} - y_{calc,i})^2}{N - P}} \quad (15)$$

where, N is the number of data points, and P is the number of parameters. χ tends to one for a good refinement. The performance of the model can also be followed by monitoring the R factor, R_{wp} which goes to a small value for a good model:

$$R_{wp} = \sqrt{\frac{\sum_{i=1}^N w_i (y_{obs,i} - y_{calc,i})^2}{\sum_{i=1}^N w_i y_{obs,i}^2}} \quad (16)$$

A space group has to be given to the model, and the right space group gives the lowest fitting value, R_{wp} . With the right space group and refined parameters, the calculated

intensities match very closely to the measured intensity peaks. In this project, Rietveld refinement is used to identify the best-fitted space group on VI_3 powder sample at high and low temperatures.

There are multiple computer programs that are used to perform the Rietveld refinement of X-ray powder data. The programs index every diffraction peak (assign each peak to a crystal plane), accounting for overlaps. The user inputs the space group and starting parameters for the lattice parameters. These lattice parameters and the other parameters mentioned above are then refined accordingly. If the space group adequately describes the diffraction pattern and the lattice parameters are reasonable, the Rietveld refinement converges to a good value of χ or R_{wp} . Otherwise, the refinement usually diverges or gives large values of χ . The model can be improved by changing the space group and using reasonable starting lattice parameters as allowed by the symmetry of the space group. In this project, the Jana2020 software package [30] was used to perform the Rietveld refinement. In the Jana2020 software, the refinement wizard allows you to perform Le-Bail refinement before carrying out the Rietveld refinement. In Le-Bail refinement, the unit cell parameters, peak width parameters and all other basic parameters are refined using the least square methods. However, the refinement does not include structural information such as fractional atomic positions and atomic site occupancy. The wizard gives a list of the best space groups that gives the best Le-Bail refinement, and the user selects one option. The refined parameters from the Le-bail refinement serve as a good starting point for carrying out the Rietveld refinement. Also, since the Le-Bail refinement does not include structural information, it usually gives a better-calculated peak profile than the Rietveld refinement. The downside is the refinement does not give the atomic positions of the atoms in the unit cell.

7 Results

7.1 Peak Splitting

This study measured long scans (18 hours) of X-ray diffraction patterns of the powdered VI_3 at 100 K, 60 K, 28 K and 12 K. In addition, short scan (2 hours) diffraction patterns of the powdered sample were also measured at various temperatures ranging from 150 K to 20 K. As reported by several studies [28][29], VI_3 is reported to undergo structural transition around 79 K. This means there is a change in the symmetry of the crystal below 79 K, and this will be shown in the diffraction pattern. The change in symmetry is manifested in the diffraction pattern by the splitting of a single peak and the sudden appearance of two or more peaks. The splitting of a peak in a diffraction pattern as the temperature is lowered is indicative of a structural transition. It suggests a rearrangement of the atoms in a unit cell. Therefore, in order to establish that there is a structural phase transition within the measured diffraction data of VI_3 , at least one peak within the X-ray pattern should split as the temperature is decreased. Both long and short scans of the powdered diffraction data show that the (300) peak splits as the temperature decreases. The image below shows the (300) peak at 12 K, 28 K, 60 K and 100 K. As shown, the peak splits into two distinct peaks at low temperatures.

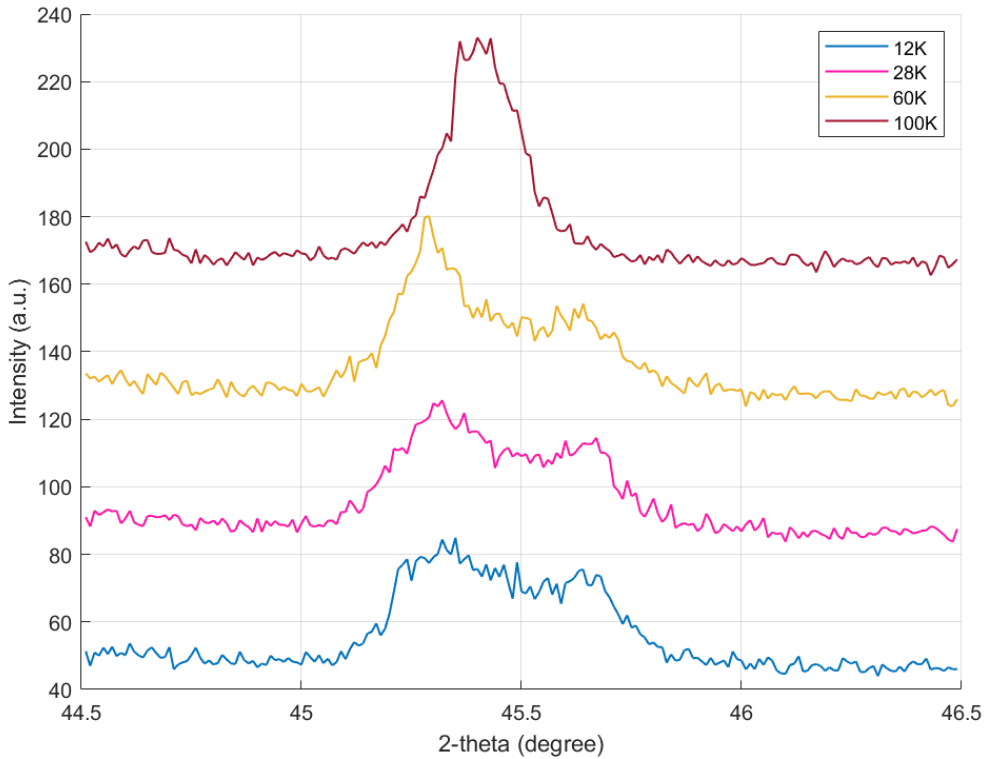


Figure 16: The (3 0 0) peak splits into two different peaks at low temperatures as a result of the change in the symmetry of the lattice.

The (300) peak was fitted by a double Lorentzian function with a linear background in each short scan diffraction pattern ranging from 150 K to 20 K. The fitting function is

given by the formula:

$$\frac{Aw}{\pi} \left(\frac{1}{w^2 + (2\theta - 2\theta_0^2)^2} \right) + \frac{Bw}{\pi} \left(\frac{1}{w^2 + (2\theta - 2\theta_1^2)^2} \right) + C2\theta + D \quad (17)$$

where A and B are the normalisation constants for the first and second peaks, respectively. w is the half-width at half-maximum, $2\theta_0$ and $2\theta_1$ are the mean 2θ position of the first and second peak, respectively. C and D are the gradient and y-intercept of the linear background, respectively. The fitting function in MATLAB returns an estimate and the associated error of the parameters: A , B , w , $2\theta_0$, $2\theta_1$, C and D for the peak. The images below show how the fitting Lorentzian function matches the X-ray data of the (300) peak.

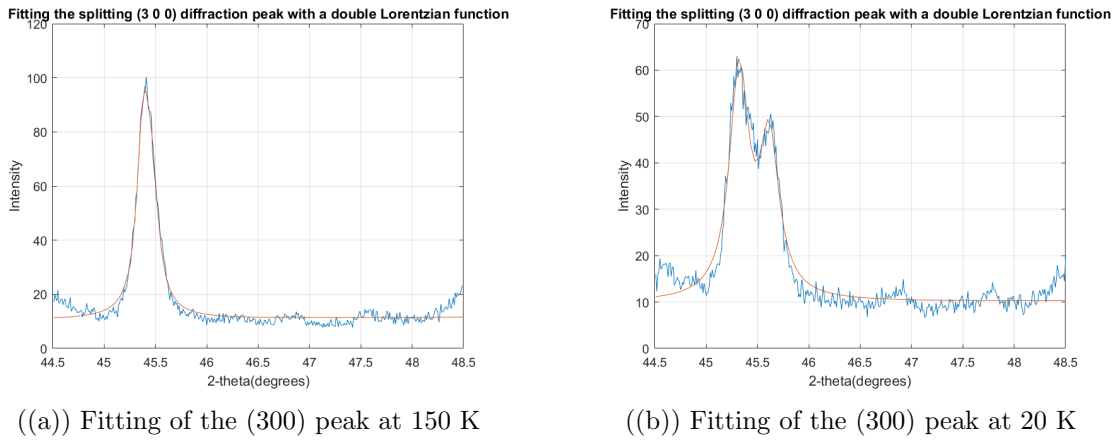


Figure 17: The red line represents the fitting Lorentzian function, and the blue line shows the X-ray diffraction data for the (300) peak.

Using the fitting Lorentzian function, the position of the two peaks that results from the sudden splitting of the (300) peak was tracked with temperature. This enabled us to roughly see what temperature range the structural phase transition occurs.

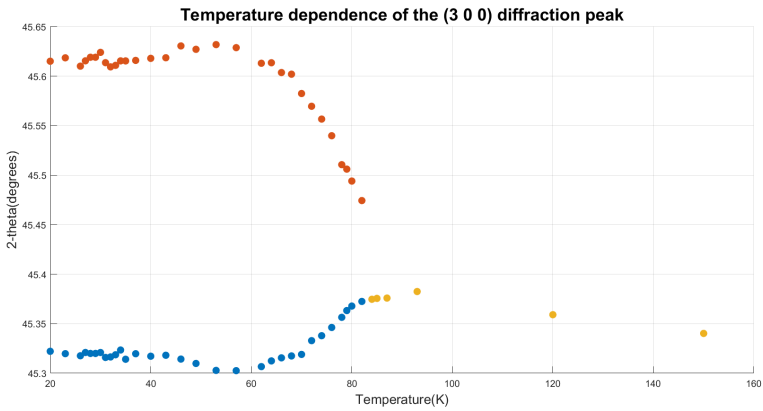


Figure 18: The yellow circles represents the (300) peak before splitting, and the blue and red circles represent the two peaks resulting from the splitting of the (300) peaks towards lower and higher diffraction angles, respectively.

From Fig.18, it is clear that one split diffraction peak moves to larger and the other moves to small 2θ values. It also shows that the structural phase transition of VI_3 occurs around 80 K, in good agreement with the reported structural phase transition temperature [28][29]. However, a few studies have reported a second structural phase transition at 32 K [27] [47]. This second phase transition was not observed in the measured X-ray diffraction patterns and hence in agreement with the other reports that also did not witness this further structural change [28] [29]. In order to gain more insight into where exactly the phase transition occurs, below is a plot of the half-width at half maximum(w) of the (300) peak and its splitting peaks with temperature.

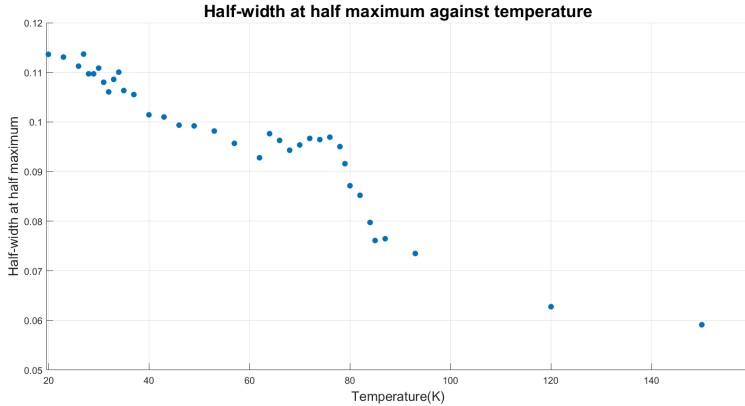


Figure 19: The fitting Lorentzian function also was used to track the half-width at half maximum of the (300) peak before and after splitting.

It must be noted from Eq.17 that w was kept the same for both splitting peaks. As seen from the image above, there is a maximum around the 80 K region, signifying an abrupt change in peak width. This provides another way of observing the structural transition and does indeed confirm that there is a structural transition around 79 K, as reported in the literature.

7.2 Crystal structure of VI_3 above the structural phase transition temperature

As established in the previous section, VI_3 has a different crystal structure above and below the structural phase transition around 79 K. Space group determination from powder diffraction data aims to determine the most likely space group consistent with the powder diffraction rather than a unique solution. This is due to the fact that the three-dimensional data of a single crystal is compressed onto the single dimension of the diffraction angle 2θ . Starting with the maximum 230 space groups, the aim is to reduce this number to a few space groups. The first step is the determination of the unit-cell geometry. The honeycomb lattice structure is typical for the mono-layer of transition metal halides with one cation surrounded by six anions to form an octahedral structure [48].

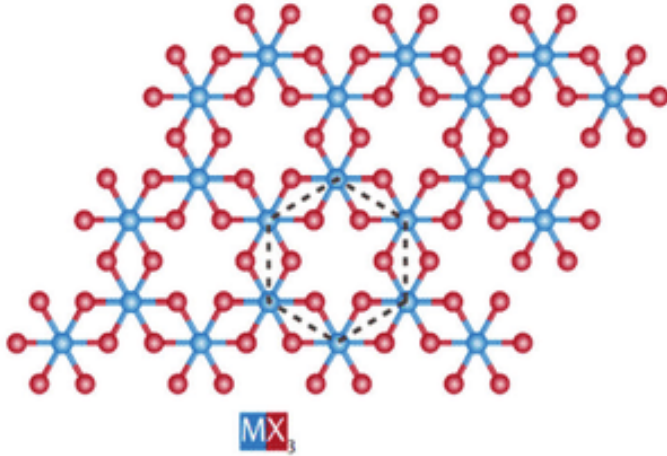
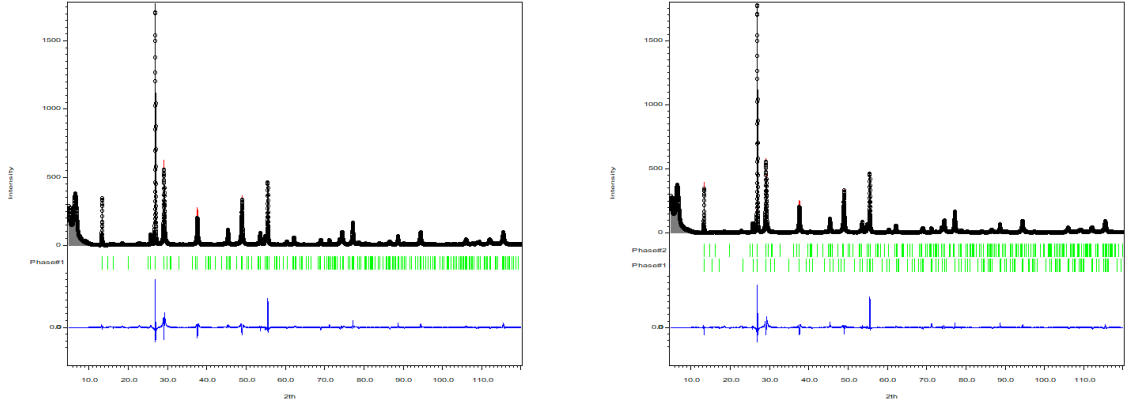


Figure 20: The common structural motif of transition metal halides is a honeycomb net of cations that are at edges sharing octahedral coordination. The blue circles represent the cations, and the red circles represent the anions [48].

The honeycomb net has a three-fold symmetry, restricting the crystal system of VI_3 at high temperature to the trigonal or hexagonal system. This reduces the number of possible space groups to forty-five space groups. So far, there have been three reported space groups of VI_3 at high temperatures(HT): $R\text{-}3(148)$, $P31c(159)$ and $C2/m(12)$. Straight away, it becomes obvious the space group at HT cannot be $C2/m$ due to the three-fold symmetry on the unit cell. In this study, the Rietveld structural refinement at 100 K was performed with the $R\text{-}3$, $P31c$ and the $C2/m$ space groups. The Rietveld refinement with the $C2/m$ space group diverged with the Jana2020 software and could not index the diffraction pattern, confirming that the high-temperature crystal structure is from the trigonal crystal family. There is another study which also tried to fit the diffraction pattern with the $C2/m$ space group[47]. They also concluded that their model does poorly with this space group. On the other hand, the structure refinement with the $R\text{-}3$ and $P31c$ space groups was very similar, with the $R\text{-}3$ space group consistently having a slightly better R_{wp} value. This is not entirely surprising as the symmetries of both space groups are very similar. Interestingly, there has been another report which suggests that the best structural fit is obtained by refining a weighted two-phase structural model containing about 25% $P31c$ phase and about 75% $R\text{-}3$ phase [49]. With this information, the Rietveld refinement at 100 K was also performed on the diffraction pattern using the $P31c$ and $R\text{-}3$ space groups. Figure 21 shows the plots of the Rietveld using only the $R\text{-}3$ space group, the $P31c$ space group and the mixture of both space groups. The table below shows the goodness of fit and the R factor for all three cases.

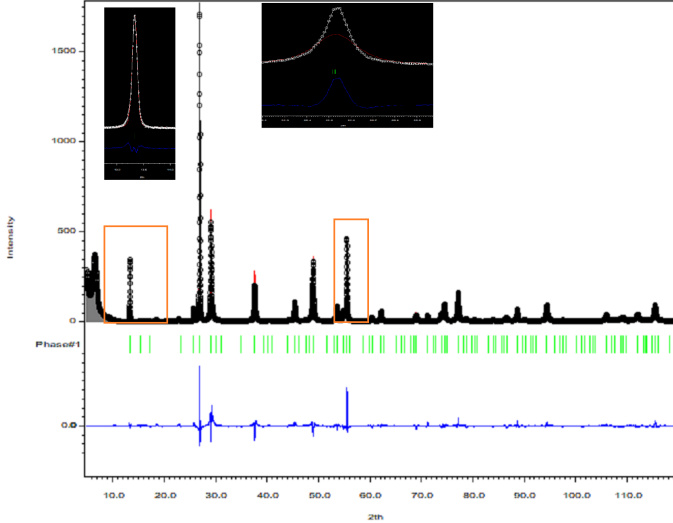
Table 1: **Performance of the Rietveld refinements at 100 K**

Space group	χ	R_{wp}
$R\text{-}3$	0.99	23.52
$P31c$	0.99	23.67
$R\text{-}3 + P31c$	0.93	22.22



((a)) Rietveld refinement with the $P31c$ space group at 100 K

((b)) Rietveld refinement using both the $R\text{-}3$ and $P31c$ space groups at 100 K



((c)) Rietveld refinement with the $R\text{-}3$ space group at 100 K

Figure 21: This is the Rietveld refinement of the powder X-ray diffraction data at 100 K. The black line represents the measured X-ray data, and the red line is the calculated intensity from the structural model. The blue line shows the difference between the measured and calculated intensities. The green lines are the miller indices index of the peaks.

As seen from Fig. 21, the performance of the Rietveld refinement in all three scenarios is very similar. From table 1, the best performing model is the refinement with the combined space groups. The proportion of the $R\text{-}3$ space group in this model is 0.77. Since the combined model did not massively improve the refinement as suggested in [49] and the $R\text{-}3$ space group is very dominant in this model, it was concluded that the $R\text{-}3$ space group best describes VI_3 at high temperatures. In addition, from table 1, it is seen that the model based entirely on the $R\text{-}3$ space group is slightly better than the model based on the $P31c$ space group.

As shown in Fig. 21(a), the calculated intensities of the Rietveld model matches the measured intensities to a good degree of accuracy for most of the peaks except for a few peaks. In particular, the (006) and (0012) peaks with 2θ values of 26.96° and 55.58° , respectively. The poor refinement of these specific peaks is also evident in the low-temperature regime, where we used a completely different Rietveld model. To verify that

the crystal structure of VI_3 does indeed belongs to the trigonal, the Rietveld refinement was done with space groups belonging to the other crystal systems. In all of these cases, the refinement either diverges or gives a very large R_{wp} value. Thus, confirming that the crystal structure of VI_3 does indeed belong to the trigonal crystal system. Among the space groups within the trigonal family, the $R\text{-}3$ space group seems to give the best model that describes the diffraction pattern. The topas refinement software[50] was also used to refine the diffraction data. This was done to check if the issue in refining these peaks originates from the Jana2020 software. Interestingly, the refinement obtained using Topas was strikingly similar to the refinement obtained from Jana, as shown in Fig.21. This suggests that the model is not accounting for an extra parameter that would help resolve the refinement of the (006) and (0012) peaks. Accounting for this extra parameter is very difficult or impossible to implement using these refinement software as almost every permutation of the available parameters was tried. The possibility of what this extra parameter/parameters may be is discussed in section 8. For a full list of the refined parameters for each model, see the Appendix section A. The goodness of fit, χ and the R factor, R_{wp} , of the $R\text{-}3$ refinement model are 0.99 and 23.52, respectively. The goodness of fit value suggests that the model overfits the data. In this particular situation, the R_{wp} value has more importance as its value highlights the few poor refinements of the model. It must be noted that none of the other space groups gives a lower R_{wp} value. The table below gives the crystallographic information obtained from the refinement.

Table 2: **Structural Parameters**

<i>R</i> -3 (148)					
<i>a</i> (Å)	<i>b</i> (Å)	<i>c</i> (Å)	α	β	γ
6.904(2)	6.904(2)	19.825(3)	90°	90°	120°
Atom	<i>x</i>	<i>y</i>	<i>z</i>	<i>Occ.</i>	<i>U_{iso}</i>
I	-0.007(1)	0.661(1)	0.420(1)	1	0.0001
V	0.333333	0.666667	0.503(7)	1	0.0001

$$\chi = 0.99 ; R_{wp} = 23.52$$

As seen from table .2, the unit cell parameters of the structural model have the threefold symmetry as expected. Occ stands for the occupation number of the atomic site, and U stands for the thermal displacement parameter. As seen, at high temperatures, the unit cell of VI_3 only contains one vanadium ion and one iodide ion. Starting with these atomic coordinates, the symmetry operations of the $R\text{-}3$ space group can be used to obtain the position of all the atoms in the crystal. Below is an image of the crystal structure of VI_3 obtained from the cell and structural parameters of the refinement model.

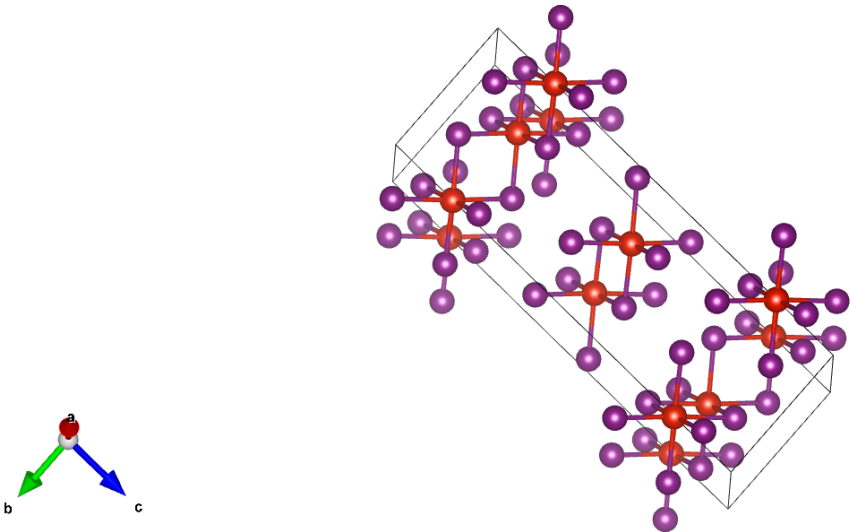


Figure 22: Crystal structure of VI_3 as obtained from Rietveld refinement. The red spheres represent the vanadium ions, and the purple spheres represent the iodide ions.

7.3 Crystal structure of VI_3 below the structural phase transition temperature

As we have already established, there is a lowering of symmetry of VI_3 from a trigonal space group. When the symmetry of a trigonal system is lowered, the crystal structure no longer has its threefold rotational symmetry axis, and the symmetry elements are reduced to a lower level. Among the crystal systems, the monoclinic and triclinic crystal systems are the only systems that can describe a reduction in symmetry from a trigonal system. The lowering of symmetry of a trigonal space group of a crystal is often assumed to be monoclinic because monoclinic is the simplest crystal system that can accommodate a reduction in symmetry from a trigonal system. In a monoclinic crystal system, the crystal has a two-fold rotational symmetry axis, which means that the crystal looks the same when rotated by 180 degrees around a specific axis. This is the simplest way to accommodate a loss of the three-fold rotational symmetry axis of a trigonal system. The reported space groups of VI_3 below the transition temperature are: $C2/m$, $C2/c(15)$, $P-1(2)$ and the $R-3$ space groups. The $R-3$ space group cannot be the crystal structure at low temperatures as it is the best-fitted spaced group at high temperatures. In this study, the powdered X-ray diffraction pattern of VI_3 at 60 K, 28 K and 12 K were each fitted by the space groups: $C2/m$, $C2/c$ and $P-1$. It was found that the monoclinic $C2/c$ space group was the best-fitted space group at each of these temperatures. This further confirmed that VI_3 does not undergo a second structural transition at 32 K as reported in two reports [27] [47].

7.3.1 Structural refinement at 60 K

The powdered X-ray diffraction pattern of VI_3 measured at 60K was fitted with the space groups: $C2/c$, $C2/m$ and $P-1$. The refinement model with the $P-1$ space group diverges with Rietfeld refinement, confirming the $P-1$ space group is not the best-fitted space group at 60 K. Figure 23 shows the Rietveld refinement using the $C2/c$ and $C2/m$ space groups. The goodness of fit, χ , and the R factor, R_{wp} of the refinement model with the

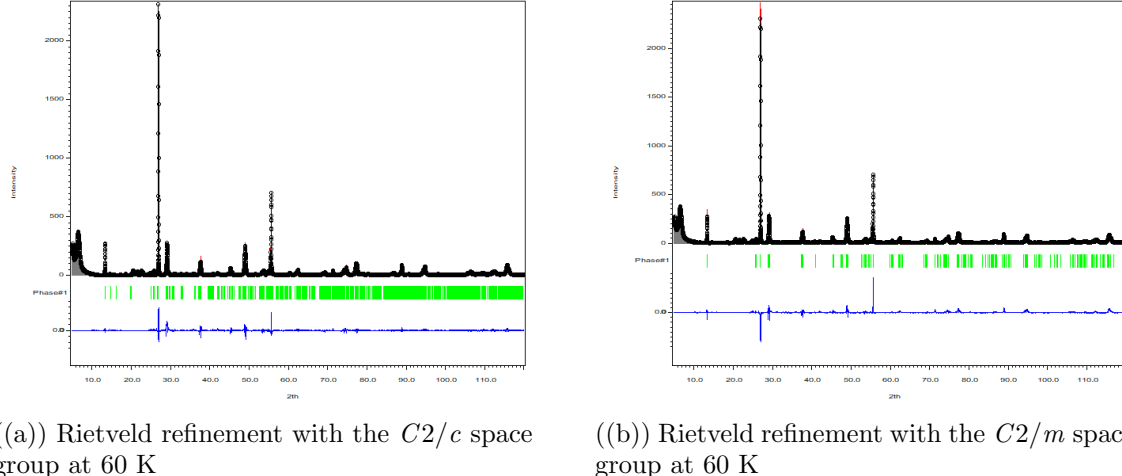


Figure 23: Rietveld refinement of the powder X-ray diffraction data at 60 K. The black line represents the measured X-ray data, and the red line is the calculated intensity from the structural model. The difference between the measured and calculated intensities is shown by the blue line. The green lines are the miller indices index of the peaks.

$C2/c$ space group are 0.99 and 25.09, respectively. Similarly, the χ and R_{wp} values of the model with the $C2/m$ space group are 1.22 and 30.87. From Fig. 23 and the R_{wp} values, it is clear that the $C2/c$ space group is the best fitting space group at 60 K, in agreement with [28]. The table below gives the full structural information of the best-fitting model.

Table 3: Structural Parameters

$C2/c(15)$					
$a(\text{\AA})$	$b(\text{\AA})$	$c(\text{\AA})$	α	β	γ
6.939(1)	11.899(2)	13.1890(5)	90°	90.443°(1)	90°
Atom	x	y	z	Occ.	U_{iso}
V	0	0.02(1)	0.75	1	0.0001
V	0	0.35(1)	0.75	1	0.0001
I	-0.19(5)	0.171(6)	0.6285(2)	1	0.0001
I	-0.15(6)	0.498(5)	0.628(2)	1	0.0001
I	0.339(6)	0.330(6)	0.628(2)	1	0.0001

$$\chi = 0.99 ; R_{wp} = 25.09$$

The structural information from table 3 shows ($\alpha = \gamma = 90^\circ$) the two-fold symmetry of the crystal below the transition temperature. As shown, the unit cell contains two vanadium ions and three iodide ions. As discussed in section 4.5, the introduction of

the distortion term in the Hamiltonian of the single vanadium ion leads to two possible ground states. The two ground states require two vanadium ions in the unit cell. Hence, the structural information of the best-fitted space group, $C2/c$, below the transition temperature confirms the prediction made by this hypothesis. Thus, the two vanadium ions in the unit cell are in different ground states.

The image below shows the crystal structure of VI_3 at 60 K using the structural information of the best-fitting model.

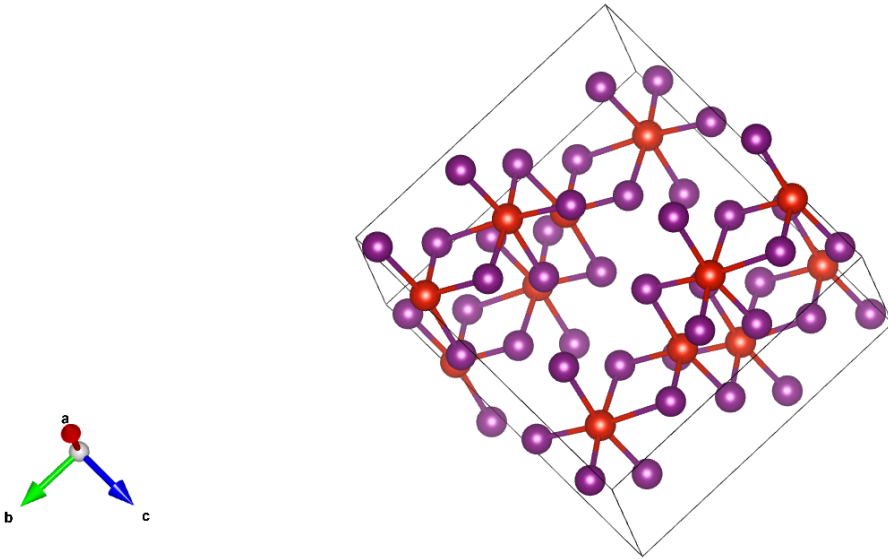


Figure 24: Crystal structure of VI_3 as obtained from the Rietveld refinement. The red spheres represent the vanadium ions, and the purple spheres represent the iodide ions.

7.3.2 Structural refinement at 28 K

Again, the Rietveld refinement of the X-ray diffraction pattern of VI_3 measured at 28 K was performed using the space groups: $C2/c$, $C2/m$ and $P-1$. So far, only one reported paper has tried to determine the space group of VI_3 below 32 K [47]. They reported a second structural phase transition in VI_3 from monoclinic to triclinic crystal structure in disagreement with our observation. They determined the $P-1$ space group as the best fitting space group below 32 K.

In contrast to the study in this report, the Rietveld refinement models based on the $C2/m$ and $P-1$ space groups diverge from the measured X-ray pattern at 28 K. This shows that the $C2/m$ and $P-1$ space groups cannot describe the position of the atoms in VI_3 . The refinement model with the $C2/c$ space group best describes the measured diffraction pattern. Figure 25 shows the Rietveld refinement of VI_3 measured at 28 K using the $C2/c$ space group. Again, this shows that VI_3 does not undergo another structural transition, and the $C2/c$ space group can be used to describe the crystal structure at all temperatures below the transition temperature. Table 4 gives the full structural information of the best refinement model at 28 K.

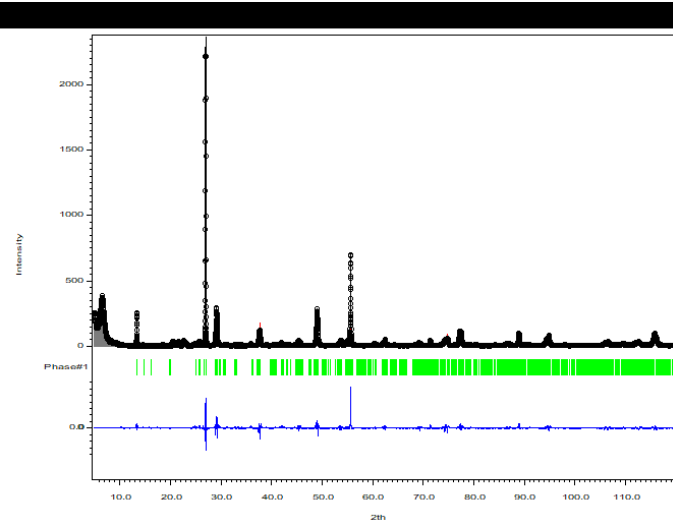


Figure 25: Rietveld refinement of the powder X-ray diffraction data at 28 K using the $C2/c$ space group. The black line represents the measured X-ray data, and the red line is the calculated intensity from the structural model. The difference between the measured and calculated intensities is shown by the blue line. The green lines are the miller indices index of the peaks.

Table 4: **Structural Parameters**

$C2/c(15)$					
$a(\text{\AA})$	$b(\text{\AA})$	$c(\text{\AA})$	α	β	γ
6.933(2)	11.906(4)	13.1850(9)	90°	90.387°(2)	90°
Atom	x	y	z	Occ.	U_{iso}
V	0	0.03(2)	0.75	1	0.0054
V	0	0.35(3)	0.75	1	0.0081
I	-0.186(8)	0.169(8)	0.629(2)	1	0.0031
I	-0.148(9)	0.495(7)	0.629(3)	1	0.003
I	0.340(8)	0.330(9)	0.630(3)	1	0.0031

$$\chi = 1.08 ; R_{wp} = 27.47$$

Again, the two vanadium ions in the unit cell confirm that there are two different ground states in the crystal structure. Figure 26 below shows the crystal structure of VI_3 at 28 K as predicted by the best fitting model.

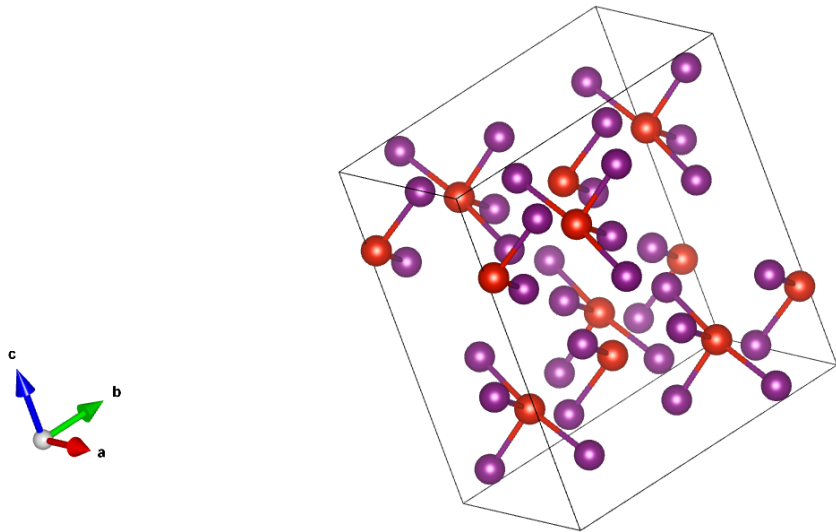


Figure 26: Crystal structure of VI_3 obtained from the Rietveld refinement at 28 K. The red spheres represent vanadium ions, and the purple ones represent iodide ions.

7.3.3 Structural refinement at 12 K

Finally, the best fitting space group on the X-ray diffraction pattern at 12 K is again the $C2/c$ space group. The $C2/m$ and $P-1$ space groups did not match the diffraction pattern very well, and in most cases, the refinement diverges. Again, this proves that VI_3 does not undergo another structural transition at low temperatures. Figure 27 shows the performance of the best-fitting model.

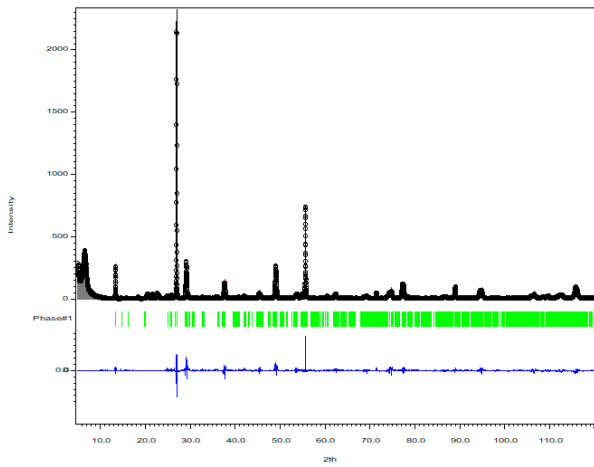


Figure 27: Rietveld refinement of the powder X-ray diffraction data at 12 K using the $C2/c$ space group. The black line represents the measured X-ray data, and the red line is the calculated intensity from the structural model. The difference between the measured and calculated intensities is shown by the blue line. The green lines are the miller indices index of the peaks.

Table 5 shows the structural information of the Rietveld refinement model.

Table 5: Structural Parameters

<i>C2/c(15)</i>					
<i>a</i> (Å)	<i>b</i> (Å)	<i>c</i> (Å)	α	β	γ
6.932(2)	11.901(4)	13.1839(8)	90°	90.38°(2)	90°
Atom	<i>x</i>	<i>y</i>	<i>z</i>	Occ.	<i>U</i>_{iso}
V	0	0.01(3)	0.75	1	0.007
V	0	0.32(4)	0.75	1	0.037
I	-0.184(8)	0.179(6)	0.629(2)	1	0.0094
I	-0.15(9)	0.500(7)	0.630(3)	1	0.021
I	0.34(1)	0.332(7)	0.628(3)	1	0.005

$$\chi = 1.15 ; R_{wp} = 28.86$$

Figure 28 shows the crystal structure of VI_3 at 12 K using the structural information from the Rietveld model.

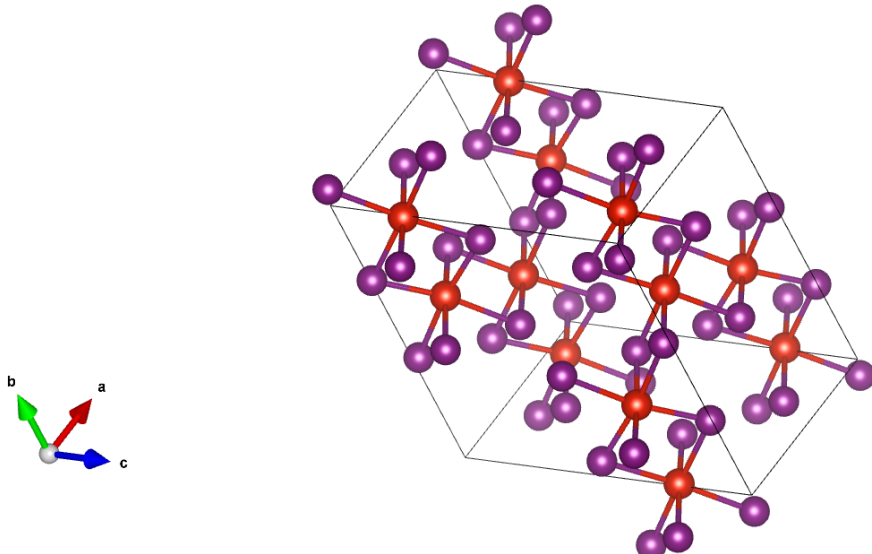


Figure 28: Crystal structure of VI_3 as obtained from the Rietveld refinement at 12 K. The red spheres represent the vanadium ions, and the purple spheres represent the iodide ions.

8 Discussion

8.1 Preferred Orientation

As seen in the refinement plots in figures 21, 23, 25 and 27, the performance of the best fitting models in matching the peaks at (006) and (0012) is poor compared to the other peaks. Figure 29 shows a magnified snapshot of the performance of the best-fitting model at 100 K. From Fig 29, it is clear that the model cannot match the measured intensity

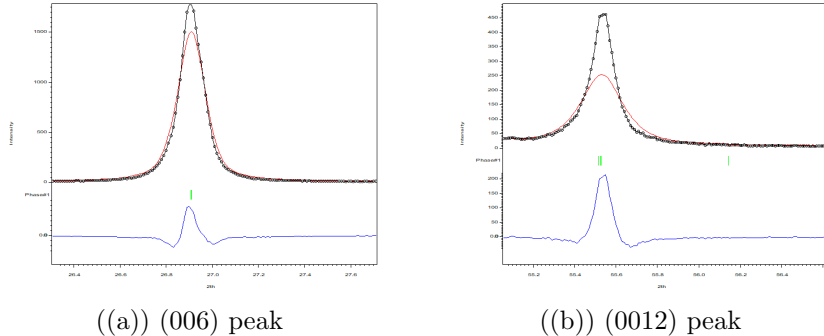


Figure 29: The matching performance of the best fitting model at 100 K on the (006) and (0012) peaks.

at these peaks. When the parameters of the model are adjusted to match these two peaks, the model does poorly on most of the other peaks in the pattern. This indicates that there is a greater intensity in the (00L) direction as a result of preferred orientation. X-ray powder diffraction relies on the crystallites having random orientations, leading to diffraction from crystal planes in a randomised manner. This way, the relative intensity between peaks can be directly related to the structural factor, leading to a better-performing model. However, when the sample has a preferred orientation, most of the crystallites lie in the same direction, leading to most of the diffraction coming from a particular crystal plane. In the case of this experiment, the preferred crystal planes were the (00L) planes. The Jana software package has a parameter that accounts for preferred orientation. It was evident during the refinement processes that this parameter significantly changes the outcome of the models. That is, all the models perform poorly when the preferred orientation parameter is not included. Despite this, the (006) and (0012) peaks were not able to be refined to a high level of accuracy. This lead to the conclusion that the mismatch in the (00L) peaks cannot be fully accounted for by the software. The best-fitting space groups determined from the measured X-ray powder diffraction will perform even better when used to refine a better sample.

The cause of the preferred orientation in the sample occurred during the grinding process. The VI_3 sample was difficult to grind due to its layered nature. The different layers slid underneath each other when pressure was applied, and to grind the sample to crystallites, the grinding had to be done in a specific orientation, leading to the preferred orientation. To improve on this project, the effects of the preferred orientation can be diminished by using an X-ray diffractometer with a transmission geometry. This setup rotates the sample as the diffraction pattern is being measured, averaging out the effect of the preferred orientation.

9 Conclusion

In this project, it was found that the room temperature crystal system of VI_3 from powder X-ray diffraction data is the trigonal structure, which is in agreement with most literature sources [24][28][29]. The best fitting space group at high temperatures is the $R\text{-}3$ space group, which has also been reported in [29]. The trigonal structure of VI_3 remains the same as temperature decreases down to about 80 K, as evidenced by the unchanged diffraction patterns. As seen from Fig 18, the relationship between temperature and the diffraction angles, 2θ , between 150 K and 80 K, is almost linear.

A structural transition is observed between 80 K and 78 K as seen by the sudden splitting of the (300) peak in Fig 18. This structural transition is described by the lowering of symmetry of the crystal structure of VI_3 , from the high-temperature trigonal structure to the low-temperature monoclinic structure. The transition is characterised by the disappearance of the (300) peak and appearing of two monoclinic peaks at different 2θ positions. This structural transition around 80 K has recently been reported in the literature, where they also measured an anomaly in the specific heat capacity of the material [28][27]. The $C2/c$ space group was found to be the best fitting space group for VI_3 at all temperatures below the transition temperature. The structural information of the $C2/c$ refinement model at low temperatures requires two vanadium ions in the unit cell. This agrees with the prediction made by the Hamiltonian of the vanadium ions. The confirmation of the hypothesis suggests that there is a link between the crystal structure of VI_3 and its magnetic properties that needs to be explored further. This might lead to useful applications whereby the magnetism can be tuned by using strain to adjust the crystal structure.

Around 50 K, VI_3 is reported to transition into the ferromagnetic phase, and this can be observed by the subtle distortion in the 2θ values around 50 K in Fig 18. The spontaneous appearance of magnetic order around 50 K is caused by the spin-orbit coupling in the Hamiltonian of the vanadium ions [42]. However, the ferromagnetic phase of VI_3 does not cause any symmetry breaking, as no peak splitting was observed within this range. The connection between the structural transition and the magnetic phenomena suggests a considerable role in spin-orbit interactions in the compound. Again, this serves as a motivation for future experiments focused on the microscopic magnetic aspect of VI_3 . This will enable a full understanding of the link between the crystal structure and the magnetic phenomena.

It has been reported in some papers that VI_3 undergoes another structural transition around 32 K [27] [47]. This second transition was not observed in the measured diffraction patterns ranging from 150 K to 12 K, in agreement with some reports [28][29].

In conclusion, this report helped clarify the confusion about the crystal structure of VI_3 by checking the performance of all the reported crystal structures at all temperatures. It was observed that VI_3 undergoes only one structural transition around 80 K. The high-temperature structure is trigonal, with the best fitting space group being $R\text{-}3$. VI_3 transitions into the lower symmetry monoclinic structure below 80 K. The best fitting space group in the low-temperature regime is the $C2/c$ space group. The spin-orbit coupling is responsible for the ferromagnetism in the compound. This report achieved its aim by helping clarify the crystal structure of VI_3 at all temperatures.

References

- [1] Tom Vincent et al. “Opportunities in electrically tunable 2D materials beyond graphene: Recent progress and future outlook”. In: *Applied Physics Reviews* 8.4 (2021), p. 041320.
- [2] Karim Khan et al. “Recent developments in emerging two-dimensional materials and their applications”. In: *Journal of Materials Chemistry C* 8.2 (2020), pp. 387–440.
- [3] Michael Ashton et al. “Topology-scaling identification of layered solids and stable exfoliated 2D materials”. In: *Physical review letters* 118.10 (2017), p. 106101.
- [4] Gowoon Cheon et al. “Data mining for new two-and one-dimensional weakly bonded solids and lattice-commensurate heterostructures”. In: *Nano letters* 17.3 (2017), pp. 1915–1923.
- [5] Sébastien Lebègue et al. “Two-dimensional materials from data filtering and ab initio calculations”. In: *Physical Review X* 3.3 (2013), p. 031002.
- [6] Nicolas Mounet et al. “Two-dimensional materials from high-throughput computational exfoliation of experimentally known compounds”. In: *Nature nanotechnology* 13.3 (2018), pp. 246–252.
- [7] K S Novoselov et al. “2D materials and van der Waals heterostructures”. In: *Science* 353.6298 (2016), aac9439.
- [8] KS Novoselov et al. “Electronic properties of graphene”. In: *physica status solidi (b)* 244.11 (2007), pp. 4106–4111.
- [9] W Rüdorff. “Graphite intercalation compounds”. In: *Advances in Inorganic Chemistry and Radiochemistry*. Vol. 1. Elsevier, 1959, pp. 223–266.
- [10] Deji Akinwande et al. “A review on mechanics and mechanical properties of 2D materials—Graphene and beyond”. In: *Extreme Mechanics Letters* 13 (2017), pp. 42–77.
- [11] Manish Chhowalla, Debdeep Jena, and Hua Zhang. “Two-dimensional semiconductors for transistors”. In: *Nature Reviews Materials* 1.11 (2016), pp. 1–15.
- [12] Bevin Huang et al. “Layer-dependent ferromagnetism in a van der Waals crystal down to the monolayer limit”. In: *Nature* 546.7657 (2017), pp. 270–273.
- [13] Cheng Gong et al. “Discovery of intrinsic ferromagnetism in two-dimensional van der Waals crystals”. In: *Nature* 546.7657 (2017), pp. 265–269.
- [14] Zhi Wang et al. “Electric-field control of magnetism in a few-layered van der Waals ferromagnetic semiconductor”. In: *Nature nanotechnology* 13.7 (2018), pp. 554–559.
- [15] Ludovicus Josephus de Jongh. *Magnetic properties of layered transition metal compounds*. Vol. 9. Springer Science & Business Media, 1990.
- [16] Leendert Johan De Jongh and Andries Rinse Miedema. “Experiments on simple magnetic model systems”. In: *Advances in Physics* 50.8 (2001), pp. 947–1170.
- [17] B Sachs et al. “Ferromagnetic two-dimensional crystals: single layers of K_2CuF_4 ”. In: *Physical Review B* 88.20 (2013), p. 201402.

- [18] Yandong Ma et al. “Evidence of the existence of magnetism in pristine VX₂ monolayers (X= S, Se) and their strain-induced tunable magnetic properties”. In: *ACS nano* 6.2 (2012), pp. 1695–1701.
- [19] Qing Hua Wang et al. “The magnetic genome of two-dimensional van der Waals materials”. In: *ACS nano* 16.5 (2022), pp. 6960–7079.
- [20] Rudolf Peierls. “On Ising’s model of ferromagnetism”. In: *Mathematical Proceedings of the Cambridge Philosophical Society*. Vol. 32. 3. Cambridge University Press. 1936, pp. 477–481.
- [21] N David Mermin and Herbert Wagner. “Absence of ferromagnetism or antiferromagnetism in one-or two-dimensional isotropic Heisenberg models”. In: *Physical Review Letters* 17.22 (1966), p. 1133.
- [22] Lars Onsager. “Crystal statistics. I. A two-dimensional model with an order-disorder transition”. In: *Physical Review* 65.3-4 (1944), p. 117.
- [23] Fabio Martinelli. “Lectures on Glauber dynamics for discrete spin models”. In: *Lectures on probability theory and statistics (Saint-Flour, 1997)* 1717 (1999), pp. 93–191.
- [24] KO Berry, RR Smardzewski, and RE McCarley. “Vaporization reactions of vanadium iodides and evidence for gaseous vanadium (IV) iodide”. In: *Inorganic Chemistry* 8.9 (1969), pp. 1994–1997.
- [25] Shangjie Tian et al. “Ferromagnetic van der Waals crystal VI₃”. In: *Journal of the American Chemical Society* 141.13 (2019), pp. 5326–5333.
- [26] Elena Gati et al. “Multiple ferromagnetic transitions and structural distortion in the van der Waals ferromagnet VI₃ at ambient and finite pressures”. In: *Physical Review B* 100.9 (2019), p. 094408.
- [27] Petr Doležal et al. “Crystal structures and phase transitions of the van der Waals ferromagnet VI₃”. In: *Physical Review Materials* 3.12 (2019), p. 121401.
- [28] Suhan Son et al. “Bulk properties of the van der Waals hard ferromagnet VI₃”. In: *Physical Review B* 99.4 (2019), p. 041402.
- [29] Tai Kong et al. “VI₃—a new layered ferromagnetic semiconductor”. In: *Advanced Materials* 31.17 (2019), p. 1808074.
- [30] Václav Petříček, Michal Dušek, and Lukáš Palatinus. “Crystallographic computing system JANA2006: general features”. In: *Zeitschrift für Kristallographie-Crystalline Materials* 229.5 (2014), pp. 345–352.
- [31] Ingo Loa. *Introduction to Condensed Matter Physics Lecture Notes*. Vol. 1. University of Edinburgh, 2022.
- [32] Charles Kittel. “Introduction to solid state physics Eighth edition”. In: (2021).
- [33] Jeremy Karl Cockcroft. *Instrument X-ray Optics. Reflection Geometry* = <http://pd.chem.ucl.ac.uk/pdnn/inst1/optics1.htm>, note = Accessed: 15-03-2023, year = 1997-2006, organization = Birkbeck College, University of London.

- [34] The Editors of Encyclopaedia. Britannica. “*bremssstrahlung*” = <https://www.britannica.com/science/bremssstrahlung>, note = Accessed: 15-03-2023, organization = Encyclopedia Britannica.
- [35] Jeremy Karl Cockcroft. *Generation of X-rays* = <http://pd.chem.ucl.ac.uk/pdnn/inst1/xrays.htm>, note = Accessed: 15-03-2023, year = 1997-2006, organization = Birkbeck College, University of London.
- [36] Kannan M Krishnan. *Principles of Materials Characterization and Metrology*. Oxford University Press, 2021.
- [37] J Katsaras et al. “Neutron and X-Ray Scattering from Isotropic and Aligned Membranes”. In: *Structure and Dynamics of Membranous Interfaces* (2008), pp. 107–134.
- [38] Paul Barnes. *Symmetry* = <http://pd.chem.ucl.ac.uk/pdnn/diff2/loren.htm>, note = Accessed: 15-03-2023, year = 1997-2006, organization = Birkbeck College, University of London.
- [39] G Caglioti, A t Paoletti, and FP Ricci. “Choice of collimators for a crystal spectrometer for neutron diffraction”. In: *Nuclear Instruments* 3.4 (1958), pp. 223–228.
- [40] Jeremy Karl Cockcroft. *Symmetry* = <http://pd.chem.ucl.ac.uk/pdnn/symm1/symintro.htm>, note = Accessed: 15-03-2023, year = 1997-2006, organization = Birkbeck College, University of London.
- [41] David Moss Jeremy Karl Cockcroft Huub Driessen. *Symmetry* = <http://pd.chem.ucl.ac.uk/pdnn/symm2/define1.htm>, note = Accessed: 15-03-2023, year = 1997-2006, organization = Birkbeck College, University of London.
- [42] Chris Stock et al. “Two-dimensional ferromagnetic spin-orbital excitations in honeycomb VI 3”. In: *Bulletin of the American Physical Society* (2023).
- [43] Ke Yang et al. “VI 3: A two-dimensional Ising ferromagnet”. In: *Physical Review B* 101.10 (2020), p. 100402.
- [44] Chengxi Huang et al. “Discovery of twin orbital-order phases in ferromagnetic semiconducting VI 3 monolayer”. In: *Physical Chemistry Chemical Physics* 22.2 (2020), pp. 512–517.
- [45] Peter Luger. *Modern X-ray analysis on single crystals*. de Gruyter, 1980.
- [46] John SO Evans and Ivana Radosavljevic Evans. “Structure analysis from powder diffraction data: Rietveld refinement in excel”. In: *Journal of Chemical Education* 98.2 (2020), pp. 495–505.
- [47] Thomas Marchandier et al. “Crystallographic and magnetic structures of the V I 3 and LiV I 3 van der Waals compounds”. In: *Physical Review B* 104.1 (2021), p. 014105.
- [48] Shengxue Yang, Tianle Zhang, and Chengbao Jiang. “van der Waals magnets: Material family, detection and modulation of magnetism, and perspective in spintronics”. In: *Advanced Science* 8.2 (2021), p. 2002488.
- [49] Sanja Djurdjić Mijin et al. “Short-range order in VI3”. In: *Inorganic Chemistry* 59.22 (2020), pp. 16265–16271.

- [50] Coelho Software. *TOPAS-Academic V7* = http://www.topas-academic.net/Technical_Reference.pdf. Accessed: 15-03-2023. 2020.

Appendices

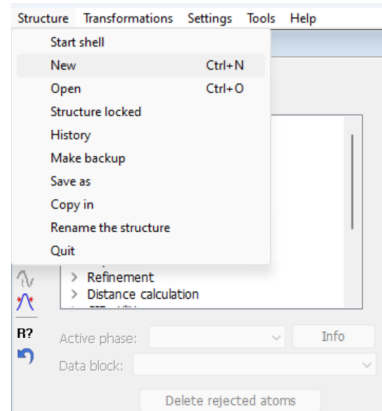
A Steps of performing Rietveld refinement with Jana2020 for 100K X-ray data

The refinement process outlined below was used to obtain the refinements at the other temperatures.

1. Click on structure

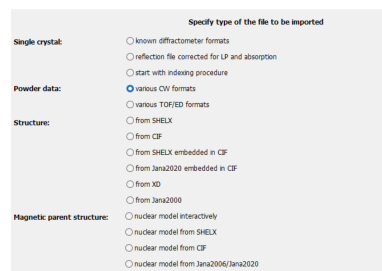
Click on New

Select X-ray data



2. Select Powder data: various CW formats

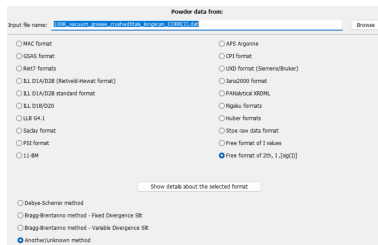
Click Next



3. Select Bragg-Brentano method -Fixed Divergence Slit

Make sure the name of the input file is right

Click Next



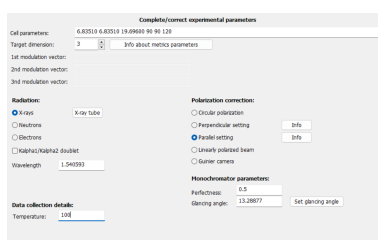
4. Enter the cell parameters and specify the temperature at which the data was collected.

Click Next

Click Finish

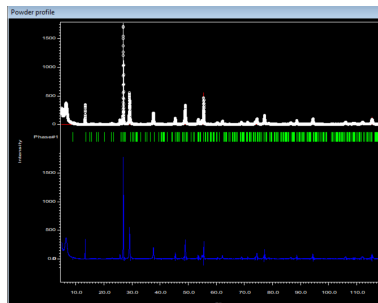
Click OK

Click OK to "Yes, I would like to continue with the wizard"

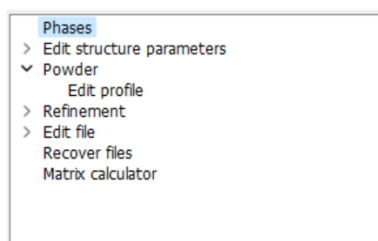


5. This is the beginning of the Le-Bail refinement.

The diffraction pattern below shows the measured intensity(white), the calculated intensity(red) and the difference between them(blue)



6. Click on Powder and double click on profile



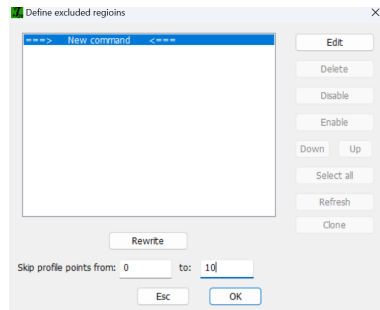
7. Within Edit profile, click on the "Corrections tab" and click on "Define excluded regions".

Enter the region to exclude and click on Rewrite.

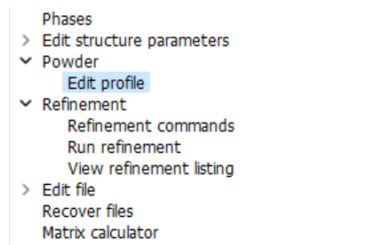
Click OK

Click OK.

Click OK to "Rewrite these files".



8. Next, run the first Le-Bail refinement by clicking on the "Refinement" and then click on "Run refinement".



9. Next, Click on Edit profile

Refine shift in the corrections tab.

Also, click on the Profile tab and select Pseudo-Voigt.

Refine GW

Run refinement

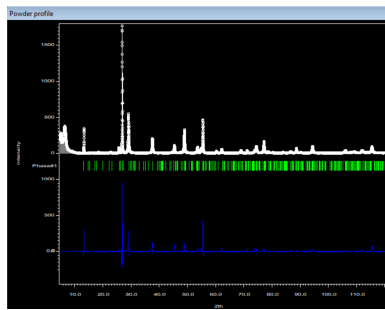
The R_{wp} value after refinement is 49.32

((a))

((b))

10. Click on Edit Profile

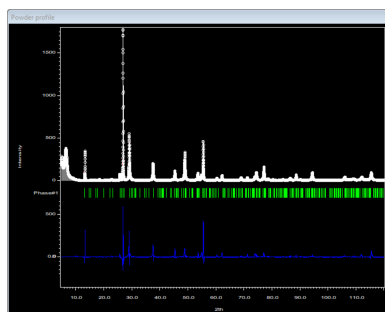
Refine GW and LX in the Profile tab



Refine shift in the Corrections tab

Run refinement

The R_{wp} value after refinement is 45.30



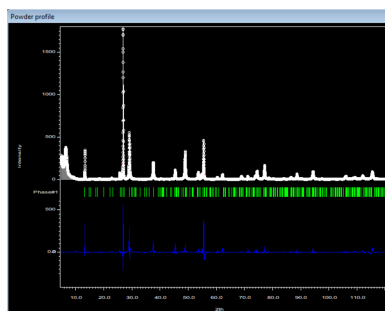
11. Click on Edit Profile

Refine GW , LX and LY in the Profile tab

Refine shift in the Corrections tab

Run refinement

The R_{wp} value after refinement is 40.81



12. Click on Edit Profile

Refine GW , LX and LY in the Profile tab

Refine shift in the Corrections tab

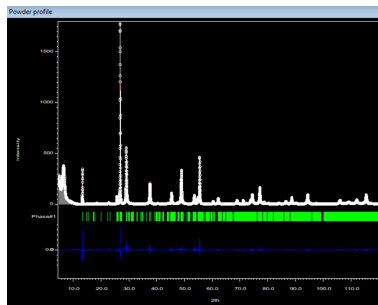
Refine a and c in the Cell tab

Run refinement

The R_{wp} value after refinement is 21.31

13. The next step is to change the space group.

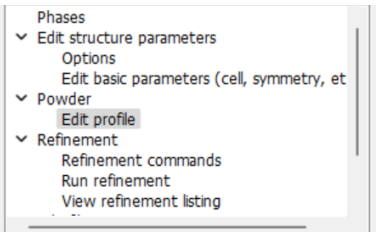
Click on Edit structure parameters



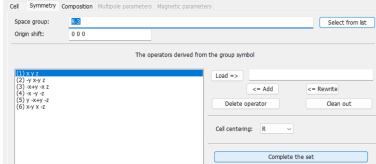
Click on Edit basic parameters.

In the Symmetry tab, change the space group to the R-3 space group

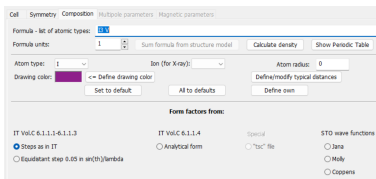
In the composition tab, enter the formula of the compound. V I3 in this case



((a))



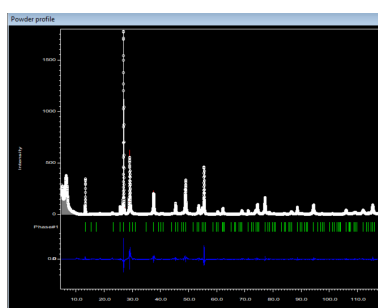
((b))



((c))

14. Next, Run the refinement with the new space group.

The R_{wp} value after refinement is 23.41



15. Next, unselect on any parameters that is being refined in the Edit profile window. Only refine the GU parameter in the Profile tab.

Run refinement

Afterwards, the unselect the GU parameter and only refine the GV parameter

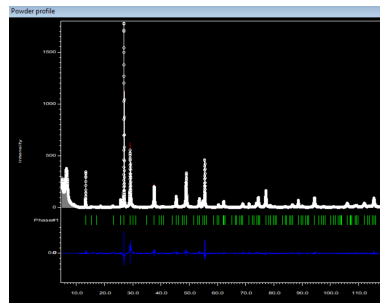
Run refinement

Unselect the GV parameter and only refine the GP parameter.

Next, unselect the GV parameter ,and click on the Asymmetry/Diffractomer tab in Edit profile. Select Berar-Baldinozzi correction and refine all four parameters. Finally, set the number of terms in the Legendre polynomial to 15. This can be done in the corrections tab.

Run refinements

The R_{wp} value after the refinements is 22.56



16. This concludes the Le-Bail refinement process.

Close the diffraction pattern to end the process. Click Next
Click Next

Select the -3 Point Group. Click Next

Select the R-observe Centering. Click Next.

Select the R-3 space group

Select "accept the space group transformed into the original cell"

Click Finish.

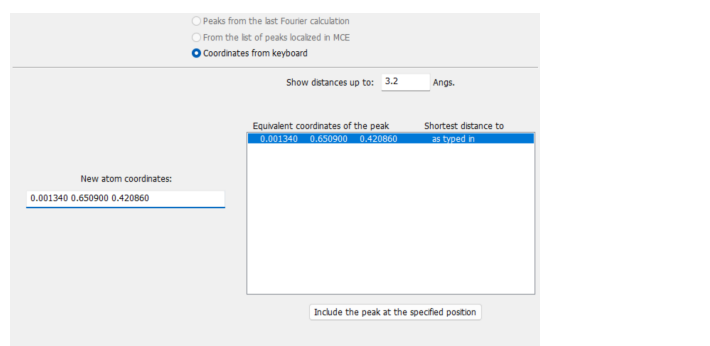
17. Quit Superflip

18. To begin the process Rietveld refinement, click on New. Then click on New atom in the dialog box on the left of the home window.

Click on "Coordinates from keyboard" in the window that pops up.

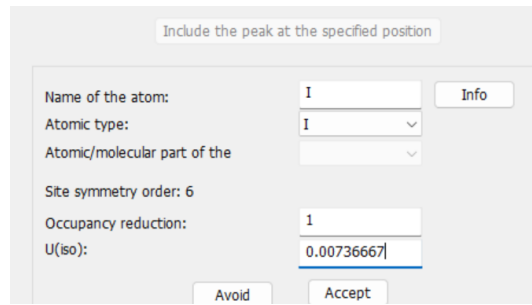
Enter the coordinates of the atoms.

Change the "show distances up to: " dialog to about 3.2



19. Next, click on "Include the peak at the specified position"

Fill in the details about the atomic type, occupation number and the U parameters.



20. Repeat the same process to add more atoms.

To view the information about the atoms, click on Edit atoms under Edit structure parameters.

Double click on any one of the atoms

Click on the Edit tab on the pop up window to view the information on the atom.

21. The following steps were taken to obtain the final Rietveld refinement.

Click on Powder. Click on Edit profile

Click on the Sample/Experiment tab. Click on March-Dollase. Select pref1. change the value from 1.1 to 0.5

Run the Rietveld refinement

Next, deselect pref1 and select pref2

Run Rietveld refinement

Deselect pref2. Select "Pitschke, Hermann and Mattern". Select rough1

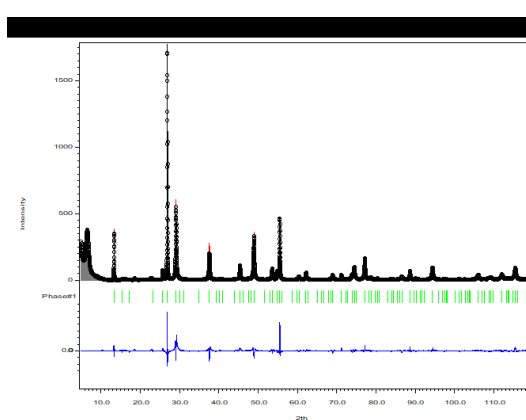
Run refinement

Deselect rough1. Select rough2

Deselect rough2. Select a and c parameters in the Cell tab.

Run refinement

This ends the refinement process.



22. Follow these steps to fix the U parameters.

Click on Refinement. Double click on Refinement commands

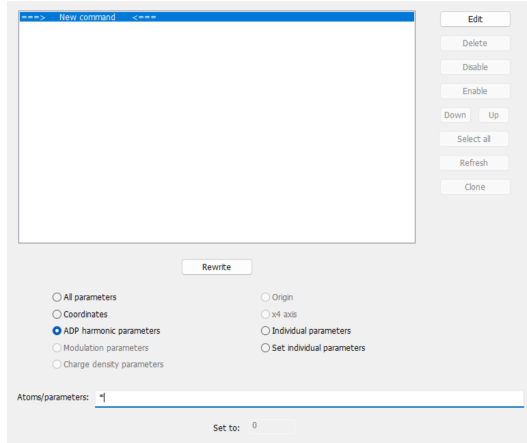
Click on the Restraints/Constraints tab

Double click Fixed commands

Select ADP harmonic parameters.

Type * into the search bar and click Rewrite.

Click OK to to overwrite the files.



B MATLAB code for tracking the temperature dependence of the splitting peak with 2θ

```
folder_path = 'C:\Users\boazm\mphys\2022_11_cool3';
%folder_path = 'C:\Users\boazm\mphys\2022_11_20';
all_files = dir(fullfile(folder_path, '*.dat'));
temps = zeros(1,(length(all_files)));
temps2 = zeros(1,(length(all_files)));
peak1 = zeros(1, length(all_files));
peak2 = zeros(1, length(all_files));
peak3 = zeros(1, length(all_files));
high_T = zeros(1, length(all_files));
width1 = zeros(1, length(all_files));
intensity1 = zeros(1, length(all_files));
intensity2 = zeros(1, length(all_files));

for i = 5:length(all_files)
    filename = all_files(i).name;
    T1 = extract(filename,57);
    T2 = extract(filename, 58);
    T3 = extract(filename, 59);
    if isnan(str2double(T3))
        T = append(T1,T2);
        T = str2double(T);
    else
        T = append(T1,T2,T3);
        T = str2double(T);
    end
end
```

```

%temps(1,i) = T;
temp2(1,i) = T;
filepath = append(folder_path , '\',filename);
filename;
delimiterIn = ' ';
headerkinesIn = 2;
data = importdata(filepath , delimiterIn , headerkinesIn );
data.data();
angles = data.data(:,1);
two_peaks_data = data.data(angles > 44.5 , :);
two_peaks_data = two_peaks_data(angles < 46.5 , :);
angles = two_peaks_data(:,1)';
intensity = two_peaks_data(:,2)';
figure(3);
plot(angles , intensity );
x0 = [45.4 ,45.5 , 0.05,20,20,10 , 0.2];
lb = [45.2 , 45.3 , 0.0001 , 0,0,0 , 0];
ub = [45.7,46,1 , 600,200,100 , 1];
x = lsqcurvefit(@lorentz_background,x0 , angles , intensity ,lb ,ub);
x
hold on
angle=linspace(angles(1),angles(end));
plot(angle,lorentz_background(x,angle));
title("Fitting the splitting (3 0 0) diffraction peak
with a double Lorentzian function);
xlabel('2-theta(degrees)');
ylabel('Intensity');
hold off
width1(1,i) = x(3);
intensity1(1,i) = x(4);
intensity2(1,i) = x(5);
if abs(x(1) - x(2)) < 0.095
    peak3(1,i) = x(1);
    high_T(1,i) = T;

else
    if x(1) < x(2)
        peak1(1,i) = x(1);
        peak2(1,i) = x(2);
        temps(1,i) = T;

    else
        peak1(1,i) = x(2);
        peak2(1,i) = x(1);
        temps(1,i) = T;

```

```

    end
end
end
temp = temps(temps^=0);

temp2 = temps2(temp2^=0);

peak1 = peak1(peak1^=0);

peak2 = peak2(peak2^=0);

width1 = width1(width1^=0);

peak3 = peak3(peak3^=0);
high_T = high_T(high_T ^= 0);

peak1;
peak2;
temp;
%plots the temperature dependence of the two splitting peaks
figure()
c = ones(1, length(peak2)).*10;
b = ones(1, length(peak3)).*10;
scatter(temp, peak1, c, 'filled');
hold on
scatter(temp, peak2, c, 'filled');
hold on
scatter(high_T, peak3, b, 'filled');
h = get(gca, 'Children');
set(h, 'FontSize', 60);
%%%%%%%%%%%%%%%
% Plots the half width at half maximum of the two splitting peaks
%scatter(temp, peak2);
%scatter([temp, temp], [peak1, peak2, c])
%plot(temp, peak1)
%plot(temp, peak2)
%scatter(temp2, width1, 'filled');

title('Temperature-dependence-of-splitting-peak');
xlabel('Temperature(K)');
ylabel('2-theta');

```

C Lorentz fitting function with linear background

```

function y = lorentz_background(x0,angle)

y = x0(4)*((1/(pi*x0(3)))*(x0(3)^2))./(((angle - x0(1)).^2)
+ (x0(3))^2) + x0(5)*((1/(pi*x0(3)))*(x0(3)^2))./(((angle - x0(2)).^2)
(x0(3))^2)+x0(7).*angle + x0(6);
end

```

D Plot of the splitting peak at 100 K, 60 K, 28 K and 12 K

```

filenames = [”C:\Users\boazm\mphys\2022_11_cool3\12K_vacuum_grease
_crushedXtals_10hscan_sample2_cool3_001.dat”,
”C:\Users\boazm\mphys\2022_11_cool3\28K_vacuum_grease_crushedXtals
_10hscan_sample2_cool3.dat”,
”C:\Users\boazm\mphys\2022_11_cool3\60K_vacuum_grease_crushedXtals
_10hscan_sample2_cool3_001.dat”,
”C:\Users\boazm\mphys\2022_11_cool3\100K_vacuum_grease_crushedXtals
_10hscan_sample2_cool3_001.dat”];

```

```

hold on
for i = 1:length(filenames)
filepath = filenames(i);
delimiterIn = ‘’;
headerkinesIn = 2;
data = importdata(filepath, delimiterIn, headerkinesIn );
angles = data.data(:,1);
two_peaks_data = data.data(angles < 46.5, :);
angles1 = two_peaks_data(:,1);
two_peaks_data = two_peaks_data(angles1 > 44.5, :);

angles = two_peaks_data(:,1)';
intensity = two_peaks_data(:,2)' + 40*i ;
plot(angles, intensity)
end
grid on

xlabel('Angle');
ylabel('Intensity');
legend('12K', '28K', '60K', '100K');

```

E Simulation of the two dimensional Ising model

```
import matplotlib
matplotlib.use( 'TKAgg' )
import sys
import math
import random
import numpy as np
import matplotlib.pyplot as plt
import matplotlib.animation as animation

# This function computes the change in energy for a Glauber dynamic
def delta_energy_glauber(spin_array , new_spin , itrial , jtrial):
    # spins of four nearest neighbours

    rows , columns = spin_array .shape

    #checking boundary conditions

    itrial_up = itrial -1
    if itrial_up == -1:
        itrial_up = rows - 1

    itrial_down = itrial + 1
    if itrial_down == rows:
        itrial_down = 0

    jtrial_left = jtrial -1
    if jtrial_left == -1:
        jtrial_left = columns -1

    jtrial_right = jtrial + 1
    if jtrial_right == columns:
        jtrial_right = 0

    #calculating energy of spin
    E_final = -J* (new_spin * spin_array [itrial_up , jtrial ])
```

```

+ new_spin*spin_array [itrial_down ,jtrial]
+ new_spin*spin_array [itrial ,jtrial_left ]
+ new_spin * spin_array [itrial ,jtrial_right ] )

old_spin = -1 * new_spin

E_initial = -J*( old_spin * spin_array [itrial_up ,jtrial]
+ old_spin*spin_array [itrial_down ,jtrial]
+ old_spin*spin_array [itrial ,jtrial_left ]
+ old_spin * spin_array [itrial ,jtrial_right ] )

E_delta = E_final - E_initial

return E_delta

```

```

J=1.0
kB = 1.0
nstep=10000

```

```

size = input(Please enter the length of the two dimensional lattice: )
try:
    size = int(size)

except ValueError:
    while type(size) != int:
        try:
            size = int(size)
        except ValueError:
            size = input(Try again! + \n +
                Please enter the length of the two dimensional
                lattice(Input must ne an integer. e.g. 50):)

T = input(Please enter the temperature of the system: )
try:
    T = float(T)

except ValueError:
    while type(T) != float:

```

```

try:
    T = float(T)
except ValueError:
    T = input(Try again! + \n
              + Please enter the temperature of the system: )

dynamic = input(Please enter the dynamics you want to use for the system.
Enter G for the Glauber method or enter K for the Kawasaki method: )
dynamic = dynamic.capitalize()
while True:
    if dynamic == "K" or dynamic == "G":
        break
    else:
        dynamic = input(Please enter the dynamics you want to use for
                      the system. Enter G for the Glauber method
                      or enter K for the Kawasaki method: )
        dynamic = dynamic.capitalize()

lx= size
ly=lx
kT = float(T)

#initialise spins randomly
spin=np.zeros((lx ,ly) ,dtype=float)
for i in range(lx):
    for j in range(ly):
        r=random.random()
        if (r <0.5):
            spin [i ,j]=-1
        if (r >=0.5):
            spin [i ,j]=1

fig = plt.figure()
im=plt.imshow(spin , animated=True)

#update loop here - for Glauber dynamics
#we are going over all elements in the 2d array n times
if dynamic == "G":
    for n in range(nstep):
        for i in range(lx):
            for j in range(ly):

```

```

#select spin randomly
    itrial=np.random.randint(0,lx)
    jtrial=np.random.randint(0,ly)
    spin_new=spin[itrial,jtrial]

#compute delta E eg via function (account for periodic BC)

    energy_diff = delta_energy_glauber(spin,
                                         spin_new,itrial,jtrial)

#perform metropolis test
    if energy_diff <= 0 :
        spin[itrial,jtrial] = spin_new
    else:
        r = random.random()
        bolt_weight = np.exp(-(1/kT)*energy_diff)
        if r <= bolt_weight:
            spin[itrial,jtrial] = spin_new

#occasionally plot or update measurements, eg every 10 sweeps
if(n%10==0):
    #update measurements
    #dump output
    f=open('spins.dat','w')
    for i in range(lx):
        for j in range.ly):
            f.write('%d %d %f\n'%(i,j,spin[i,j]))
    f.close()
    #show animation
    plt.cla()
    im=plt.imshow(spin, animated=True, vmin = -1, vmax = 1)
    plt.draw()
    plt.pause(0.0001)

if dynamic == "K":
    #looping over every element in the 2d array n times
    for n in range(nstep):
        for i in range(lx):
            for j in range.ly):
                #selecting first random spin
                itrial_1=np.random.randint(0,lx)
                jtrial_1=np.random.randint(0,ly)
                spin_new_1=spin[itrial_1,jtrial_1]

```

```

#selecting second random spin
itrial_2=np.random.randint(0,lx)
jtrial_2=np.random.randint(0,ly)
spin_new_2 = -spin[itrial_2,jtrial_2]

#if both spins have the same sign,
#there is no change in energy
#and switching them will have no effect
if spin_new_1 == spin_new_2:
    continue

#I am considering the change in energy as the
#same change in energy resulting
#from doing two consecutive
#single spin flips in the Glauber dynamics

energy_diff_1 = delta_energy_glauber(spin, spin_new_1,
itrial_1, jtrial_1)

energy_diff_2 = delta_energy_glauber(spin, spin_new_2,
itrial_2, jtrial_2)

#this checks if the two selected spins are nearest
#neighbours, as there would be overcounting in the energy.
if ((itrial_1 == itrial_2) and
    abs(jtrial_1 - jtrial_2) == 1 ) or
    ((jtrial_1 == jtrial_2) and
     abs(itrial_1 - itrial_2)==1) or
    ((itrial_1 == itrial_2) and
     abs(jtrial_1 - jtrial_2) == lx -1 ) or
    ((jtrial_1 == jtrial_2) and
     abs(itrial_1 - itrial_2) == ly -1):
        energy_diff_kawa = energy_diff_1 + energy_diff_2
        - 4*J*(spin_new_1)*(spin_new_2)

#if the two particles are not nearest neighbours
else:
    energy_diff_kawa = energy_diff_1 + energy_diff_2

#perform metropolis test
spin_1 = spin[itrial_1,jtrial_1]
spin_2 = spin[itrial_2,jtrial_2]
if energy_diff_kawa <= 0:
    spin[itrial_1,jtrial_1] = spin_2

```

```

        spin [ itrial_2 , jtrial_2 ] =spin_1

else:
    r = random . random ()
    bolt_weight = np . exp( -(1/kT)*energy_diff_kawa )
    if r <= bolt_weight:
        spin [ itrial_1 , jtrial_1 ] = spin_2
        spin [ itrial_2 , jtrial_2 ] = spin_1

#occasionally plot or update measurements, eg every 10 sweeps
if (n%10==0):
#      update measurements
#      dump output
    f=open('spins.dat','w')
    for i in range(lx):
        for j in range.ly):
            f.write( '%d %d %lf\n' %(i,j,spin [ i , j ]))
    f.close()
#      show animation
    plt.cla()
    im=plt.imshow(spin, animated=True, vmin = -1, vmax = 1)
    plt.draw()
    plt.pause(0.0001)

```